Review

Routes to turbulence in Taylor–Couette flow

Daniel Feldmann[1], Daniel Borrero-Echeverry[2], Michael J. Burin[3], Kerstin Avila[4,5] and Marc Avila[1,6]

[1]University of Bremen, Center of Applied Space Technology and Microgravity (ZARM), 28359 Bremen, Germany
[2]Department of Physics, Willamette University, Salem, OR 97301, USA
[3]Department of Physics, California State University - San Marcos, San Marcos, CA 92096, USA
[4]University of Bremen, Faculty of Production Engineering, 28359 Bremen, Germany
[5]Leibniz Institute for Materials Engineering (IWT), 28359 Bremen, Germany
[6]University of Bremen, MAPEX Center for Materials and Processes, 28359 Bremen, Germany

DF, 0000-0002-6585-2875; MA, 0000-0001-5988-1090

Fluid flows between rotating concentric cylinders exhibit two distinct routes to turbulence. In flows dominated by inner-cylinder rotation, a sequence of linear instabilities leads to temporally chaotic dynamics as the rotation speed is increased. The resulting flow patterns occupy the whole system and sequentially lose spatial symmetry and coherence in the transition process. In flows dominated by outer-cylinder rotation, the transition is abrupt and leads directly to turbulent flow regions that compete with laminar ones. We here review the main features of these two routes to turbulence. Bifurcation theory rationalizes the origin of temporal chaos in both cases. However, the catastrophic transition of flows dominated by outer-cylinder rotation can only be understood by accounting for the spatial proliferation of turbulent regions with a statistical approach. We stress the role of the rotation number (the ratio of Coriolis to inertial forces) and show that it determines the lower border for the existence of intermittent laminar–turbulent patterns.

This article is part of the theme issue 'Taylor–Couette and related flows on the centennial of Taylor's seminal *Philosophical Transactions* paper (part 2)'.

1. Background

Fluid flows tend to become turbulent as their speed increases. The emergence of turbulence is characterized by erratic fluctuations of fluid velocity and pressure, which enhance dissipation and thus lead to increased energy losses. In his seminal 1923 paper, Taylor [1] computed the instability of laminar flows between co-rotating cylinders mathematically rigorously by starting from the Navier–Stokes equations. His own experimental verification of this result established hydrodynamic stability theory as a powerful tool to make accurate predictions of flow instabilities. To understand how remarkable this accomplishment is, it is necessary to review the historical background [2]. Interest in the problem of transition was spurred by Osborne Reynolds' 1883 paper on turbulence transition in pipe flow [3]. Reynolds showed experimentally that in pipes this transition is sudden and depends on the level of disturbances present in the experiment. He concluded that *the condition might be one of instability for disturbance of a certain magnitude and stable for smaller disturbances*. Despite his remark, most of the subsequent theoretical approaches to the problem of transition, such as those pioneered by Orr [4], Sommerfeld [5] and others, focused on the evolution of infinitesimal disturbances and thus failed to predict transition in pipe flow and even in the mathematically more tractable case of plane shear flow [2].

This failure of linear hydrodynamic stability theory to explain Reynolds' experiments, and the insurmountable difficulties inherent to nonlinear theories, continued to trouble the scientific community for 40 years. Then Taylor [1] made the key observation that *the study of the fluid stability when the disturbances are not considered as infinitely small is extremely difficult. It seems more promising, therefore, to examine the stability of liquid contained between concentric rotating cylinders. If instability is found for infinitesimal disturbances in this case it will be possible to examine the matter experimentally*. Taylor's proposal was motivated by Mallock's experiments in which the inner cylinder was rotated while the outer cylinder was held fixed [6]. Mallock observed that the flow was turbulent even at the lowest speeds that he considered. These observations would go on to inspire Lord Rayleigh's derivation of a criterion for the stability of rotating inviscid fluids [7]. Taylor extended Rayleigh's analysis to include viscous effects by applying Orr's framework to the Navier–Stokes equations in cylindrical coordinates, keeping curvature terms up to first order. His calculations of the onset of instability were in excellent quantitative agreement with his own laboratory experiments. He showed this for different curvatures, as determined by the radius ratio, $\eta = r_i/r_o$, where r_i and r_o are the radii of the inner (*i*) and outer (*o*) cylinder, respectively. Furthermore, the corresponding axially periodic eigenfunctions, which take on the form of toroidal vortices stacked along the axial direction, were in good agreement with his flow visualization experiments using dye injections. Taylor's analysis was able to predict the stability of the flow even in regimes where Rayleigh's theory [7] had failed, such as when the cylinders are made to counter-rotate or in experiments where the inner cylinder is made to rotate with very low velocity. More generally, Taylor's paper was also instrumental in confirming the validity of the Navier–Stokes equations, supplemented with no-slip boundary conditions (BCs), beyond the laminar regime.

An intriguing result of Taylor's 1923 analysis, supported by his experiments, was that laminar flows with a stationary inner cylinder are linearly stable. This conflicted with earlier observations by Couette [8], who observed that the torque exerted on the inner cylinder scaled linearly at low angular speeds of the outer cylinder, Ω_o, but became erratic as Ω_o was increased above a certain critical threshold, before stabilizing but exhibiting a stronger (nonlinear) scaling at even higher Ω_o. Couette's results agreed with observations by Mallock [6], who also noted that if the system was run right below the threshold for transition and a small perturbation was introduced, the torque measurements became erratic for extended periods of time before the system returned to

its initial quiescent state. This transient nature of turbulence is a hallmark of linearly stable flows (see, e.g. Avila *et al.* [9] for a recent review) and will be discussed later in §4b.

Similar experiments were carried out by Wendt [10] at even higher Reynolds numbers. Wendt also studied the effect of the end-wall conditions in his apparatus (e.g. attaching the cap at the bottom of his test section either to the inner or the outer cylinder) and showed that these could change the critical rotation rate for transition by as much as 10%. Although Taylor initially attributed the increased torque reported for flows with stationary inner cylinder by Couette, Mallock and Wendt to end-wall effects caused by the short aspect ratio, $\Gamma = h/d \lesssim 20$, of their experimental apparatus (here, h is the cylinders' height and $d = r_o - r_i$ is the gap width between them), he was later able to reproduce qualitatively their observations with a new, longer and more accurate apparatus [11]. Furthermore, Taylor showed that the transition could be triggered by purposely applying slight perturbations and that turbulence remained sustained well below the threshold for natural (unforced) transition. This bi-stability of laminar flow and turbulence at fixed Reynolds numbers, reported earlier by Reynolds for pipe flow [3], is another hallmark of linearly stable flows (e.g. [12]). Taylor also studied the effect of varying the system geometry and extrapolated his data toward the narrow gap limit, $\eta \rightarrow 1$, to infer that the critical Reynolds number for plane Couette flow (PCF) should lie between 315 and 500, which is in agreement with more recent experiments [13–15]. In the 1950s, Schultz-Grunow [16] impressively showed that if the apparatus was fabricated with stringent tolerances, laminar flow could be maintained up to Reynolds numbers exceeding 40 000, whereas if he purposely misaligned his apparatus or used cylinders that were not perfectly round, his system would transition at Reynolds numbers consistent with earlier studies [6,8,10,11].

The early work by Taylor and others made it clear that flows between concentric cylinders exhibit two distinct routes to turbulence. The differences between these routes were pinpointed in a decade-long study published by Coles [17] in 1965. In the first route, characteristic of flows dominated by inner-cylinder rotation, transition occurs via a sequence of instabilities that increase the temporal complexity of the flow and decrease its spatial symmetry. Coles characterized this sequence using hot wire anemometry and flow visualizations. For the second route, characteristic of flows dominated by outer-cylinder rotation, Coles noted that transition to turbulence is akin to that reported by Reynolds for pipe flow [3]. It is controlled by the evolution of finite-amplitude perturbations, which can cause the sudden emergence of localized turbulent domains interspersed in a laminar background. In this paper, we review previous works on the transition to turbulence in Taylor–Couette flow (TCF) and analyse them from the perspective of nonlinear dynamical systems. The main concepts are illustrated with results from new direct numerical simulations (DNS).

2. Parameter regimes of Taylor–Couette flow

Traditionally, the different dynamical regimes of TCF have been characterized in terms of two control parameters: the inner ($Re_i = u_i d/\nu$) and the outer ($Re_o = u_o d/\nu$) cylinder Reynolds number. They are based on the azimuthal velocity of each cylinder ($u_{i/o} = r_{i/o}\Omega_{i/o}$), the width of the gap (d) between the cylinders, and the kinematic viscosity (ν) of the fluid filling the gap.

An example of a stability diagram using this traditional set of parameters is shown in figure 1*a* for a system with $\eta = 0.5$. The laminar base state of the system, i.e. circular Couette flow (CCF), is linearly (centrifugally) unstable above the neutral stability curve. For a given value of Re_o, there is a critical Re_i above which the flow becomes unstable and secondary flows with increasing complexity emerge. The neutral stability curve we show here is analogous to those computed by Taylor [1], but we discretized the full Navier–Stokes equations linearized about the CCF state with a Galerkin method [18]. Transition to turbulence in the linearly unstable region (red in figure 1) is discussed in §3.

Below the neutral stability curve, CCFs are linearly stable and only finite-amplitude disturbances can trigger turbulence. Linearly stable CCF are classified into two distinct regimes with qualitatively different physics. In the linearly stable cyclonic regime (green in figure 1),
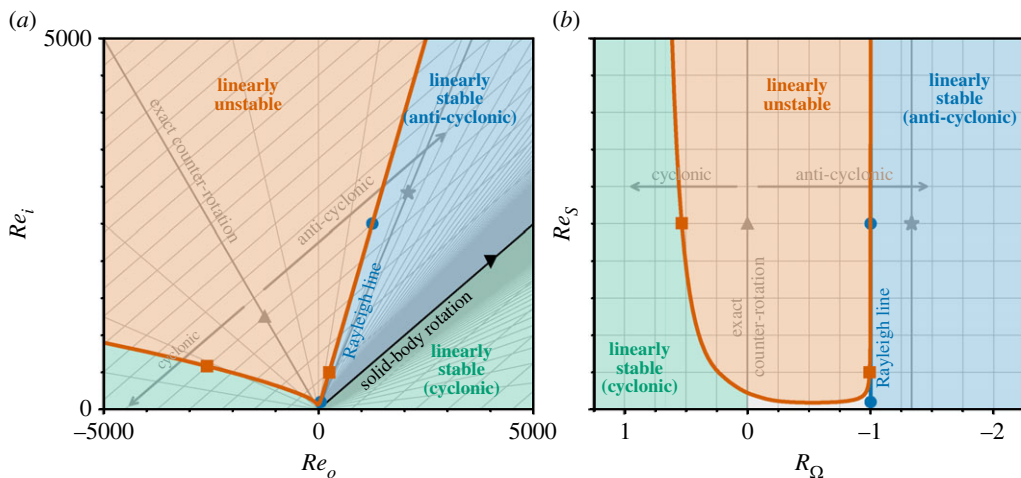
Figure 1. Parameter space of Taylor–Couette flow. (a) In terms of the inner (Re_i) and outer (Re_o) cylinder Reynolds number; here for a system with one particular curvature (radius ratio $\eta = 0.5$). Above the neutral stability curve (red lines with squares), the laminar flow is linearly (centrifugally) unstable. In the co-rotating regime, the Rayleigh line ($Re_i = Re_o/\eta^2$, blue lines with circles) is indistinguishable from the neutral stability curve (at this scale). For the specific case of solid-body rotation ($Re_i = Re_o/\eta$, black line with inverted triangle), the flow has a constant angular velocity. Stable flows to the left of this line are anti-cyclonic, and cyclonic to the right. The specific case of exact counter-rotation (grey line with upright triangle) also separates the cyclonic from the anti-cyclonic regime. (b) Same as in (a) but in terms of the shear Reynolds number (Re_S) and the rotation number (R_Ω). Here, exact counter-rotation (zero mean rotation) corresponds to $R_\Omega = 0$, the Rayleigh line is given by $R_\Omega = -1$ (in blue), Keplerian flow is best approximated with $R_\Omega = -4/3$ (grey line with star), and solid-body rotation is approached for $R_\Omega \to \pm\infty$, when coming from the cyclonic ($+$) or the anti-cyclonic side ($-$), respectively. (Online version in colour.)

the vorticity of the flow and the mean angular velocity are aligned. Here, the flow may exhibit a subcritical transition to turbulence. This transition scenario is reviewed in §4. The linearly stable anti-cyclonic or quasi-Keplerian (QK) regime (blue in figure 1) is characterized by radially increasing angular momentum, but radially decreasing angular velocity. As reviewed in §5, the weight of evidence suggests that in this regime no transition to turbulence occurs even at Reynolds numbers exceeding a million.

In 2005, Dubrulle *et al.* [19] introduced an insightful alternative parametrization of TCF, which has improved our understanding of the physics of the system and embeds it in a much wider context of general rotating shear flows. For example, their parametrization offers a simple relation to situate typical astrophysical (Keplerian) flows in the parameter space of TCF. Essentially, they defined a shear Reynolds number (Re_S) and a rotation number (R_Ω) in such a way that they translate to the traditional set of TCF parameters as

$$Re_S = \frac{2\,|\eta Re_o - Re_i|}{1 + \eta} \quad \text{and} \quad R_\Omega = \frac{(1 - \eta)(Re_i + Re_o)}{\eta Re_o - Re_i},$$

respectively. We stress that now the ratio of inertial to viscous forces and the ratio of Coriolis to inertial forces can be independently measured/controlled via Re_S and R_Ω, respectively.

Figure 1b shows the same diagram as discussed before, but in terms of R_Ω and Re_S. This representation has the advantage that some of the important regime boundaries (except for the neutral stability curve) remain unchanged as η is varied. Crucially, the line corresponding to exact counter-rotation ($R_\Omega = 0$) separates cyclonic ($R_\Omega > 0$) from anti-cyclonic ($R_\Omega < 0$) flows and smoothly connects TCF to rotating plane Couette flow (RPCF) in the limit of vanishing curvature ($\eta \to 1$). Hence, RPCF is just a specific (limiting) configuration of TCF [20]. Note that $Re_S = 4Re$, where Re is the usual Reynolds number for PCF, which is defined with the wall velocity and half the gap width. The stability boundary derived by Rayleigh [7] for inviscid fluids (i.e.

the Rayleigh line) is at $R_\Omega = -1$. Solid-body rotation can be approached from the cyclonic side ($R_\Omega \to \infty$) or from the anti-cyclonic side ($R_\Omega \to -\infty$). In (Re_i, Re_o)-space, however, these curves all depend on η and thus move around as the curvature of the system is varied. This makes the comparison of results obtained for different geometries more challenging.

Before discussing transition in the different regions, it is important to point out that all the curves shown in figure 1, as well as their stability properties, were defined (or computed) under the assumption of an ideal (pure rotary) CCF as base state. In laboratory experiments, however, perfect CCF cannot be attained because of the axial end-walls that confine the flow in axial direction and spawn secondary flows. Hence, Γ and the specific end-wall conditions used in laboratory experiments are additional important variables that need to be considered when comparing results from different Taylor–Couette simulations and experiments.

3. Supercritical route to turbulence

TCF is least stable when the outer cylinder is held stationary ($Re_o = 0$), as noted early on by Mallock [6]. He reported turbulent flow for all rotation speeds of the inner cylinder that he could achieve in his experiments. In fact, the minimum realizable rotation speed in his apparatus already resulted in a supercritical Reynolds number (as shown later by Taylor [1]). Flows with stationary inner cylinder have attracted a lot of interest [21] because they simplify the experimental setup considerably. In this section, we review the transition to turbulence for $\eta = 0.875$ and $Re_o = 0$ as Re_i is increased from 100 to 4000. Our choice is motivated by the influential experimental investigation of Gollub & Swinney [22], who measured time series of the radial velocity (u_r) at mid gap and revealed three distinct instabilities, each adding a new frequency to the Fourier spectrum of u_r as Re_i was increased. In a further transition, the flow was shown to exhibit a continuous spectrum characteristic of chaotic dynamics, in apparent agreement with a theorem by Ruelle & Takens [23] regarding the existence of chaotic dynamics near three-tori in dynamical systems. Here, we present new computational results to illustrate the transition process.

To this end, periodic BC are employed in the axial (z) and azimuthal (θ) direction and simulations of the incompressible Navier–Stokes equations carried out using our pseudo-spectral DNS code `nsCouette` [24]. The highest friction Reynolds number ($Re_\tau = u_\tau d/\nu$) measured in all DNS presented here amounts to 95.7, where u_τ is the friction velocity at the inner cylinder wall. We used a spatial resolution (in terms of viscous wall-units based on Re_τ and denoted by $^+$) of at least $0.02 \le \Delta r^+ \le 1.3$, $\Delta\theta r_i^+ = 3.8$ and $\Delta z^+ = 3.5$, which is the state of the art in DNS of wall-bounded turbulence [25,26]. In `nsCouette`, the size of the time step is dynamically adapted during run time to ensure numerical stability and lies between 5×10^{-7} and 5×10^{-6} viscous time units (d^2/ν) for all DNS presented here (depending on the exact setup). Except for the spiral turbulence simulation presented in §4a, all DNS were run for at least $20\,d^2/\nu$, before data were recorded and analysed.

(a) Bifurcation cascade to temporal chaos

We begin by examining the onset of temporally chaotic dynamics in a small computational domain with axial aspect ratio $\Gamma = 5/2$ and only one quarter of the circumference in the azimuthal direction ($\theta \in [0, L_\theta]$ with $L_\theta = \pi/2$). This choice is made to match the sequence of patterns reported by Gollub & Swinney [22] for a system with $\eta = 7/8$ and $\Gamma \approx 20$. In their experiments, the primary instability took the form of Taylor vortices (TV) with an axial wavelength of approximately $(5/2)d$, corresponding to eight pairs of vortices stacked upon each other in their apparatus. Our simulations with $\Gamma = 5/2$ are expected to capture the dynamics of two counter-rotating TV around the central section of their experiments, where the flow patterns are approximately periodic in z [22]. A summary of the flow patterns, dynamics and regimes as Re_i is increased in our simulations is presented in figure 2 and detailed below.
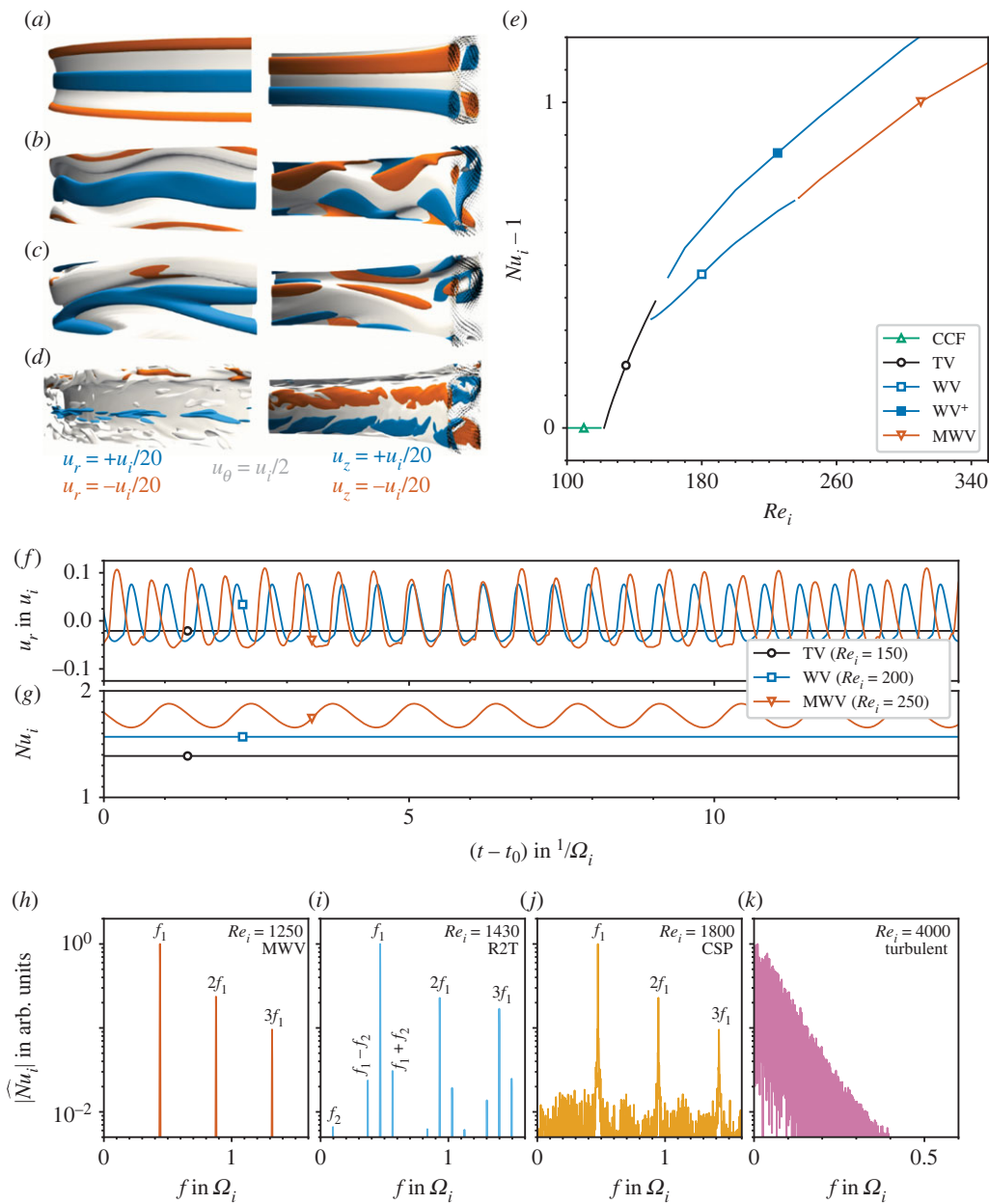
Figure 2. Route to turbulence in Taylor–Couette flow with stationary outer cylinder ($Re_o = 0$) as the inner cylinder Reynolds number (Re_i) is increased from 100 to 4000 in our simulations for fixed $\eta = 7/8$, $\Gamma = 5/2$ and $L_\theta = \pi/2$. (a)–(d) Visualizations of colour-coded iso-contours of the radial (u_r), azimuthal (u_θ) and axial (u_z) velocity components show that the spatial structure of the flow field becomes progressively more complex as Re_i increases from (a) $Re_i = 150$ (Taylor vortex, TV) to (b) $Re_i = 200$ (wavy vortex, WV) to (c) $Re_i = 250$ (modulated wavy vortex, MWV) and finally to (d) $Re_i = 4000$ (turbulent flow). (e) Nusselt number of the inner cylinder (Nu_i) as a function of Re_i for the different flow states of increasing complexity starting with circular Couette flow (CCF). (f)–(g) Time series of u_r (recorded at mid gap) and Nu_i for selected states. (h)–(k) Power spectra of the time series of Nu_i for selected states including a relative two-torus (R2T) and a chaotic state exhibiting a continuous spectrum with peaks (CSP). (Online version in colour.)

At $Re_i \approx 122$ the CCF becomes unstable and is replaced by one pair of axisymmetric TV, visualized in figure 2a for the example of $Re_i = 150$. In this transition, the invariance of CCF to axial translations is broken, while its rotational symmetry and its axial reflection symmetry (about the vertical mid plane) are preserved. The TV state is stationary, as can be seen in the time series of u_r recorded at mid-gap position (figure 2f) and in the time series of the inner-cylinder Nusselt number (Nu_i) as well (figure 2g). The latter represents the torque that is necessary to rotate the inner cylinder for a given flow state, normalized by the torque that would be required for CCF at the same Re_i.

Flow transitions, and more generally turbulence and transition, can be analysed from a dynamical systems perspective [27]. In this framework, the Navier–Stokes equations span an infinite-dimensional phase space consisting of all admissible flow fields (i.e. satisfying mass and momentum conservation). Here, time-dependent flows correspond to trajectories, whereas time-independent flows, like the TV flow, correspond to steady states or fixed-points in that phase space. The emergence of a new stable fixed-point (TV), which bifurcates from an existing one (CCF) that loses its stability, corresponds to a qualitative change in phase space or bifurcation. The bifurcation diagram in figure 2e captures this transition. Note that if TV is shifted axially by an arbitrary amount, the shifted TV pattern is still a solution to the system, so this bifurcation is known as a *pitchfork of revolution*. For a more detailed treatment, the reader is referred to Kuznetsov [28] for an introduction to bifurcation theory, to Chossat & Lauterbach [29] for a discussion of equivariant bifurcation theory, to Chossat & Iooss [30] for its application to TCF, and to Crawford & Knobloch [31] for a review of symmetry-breaking bifurcations in fluid dynamics.

As the inner cylinder is further accelerated beyond $Re_i \approx 150$, the TV state turns unstable and the flow field becomes three-dimensional and time-dependent [17]. As shown in figure 2b, the vortices acquire waviness in θ, breaking the rotational and the axial reflection symmetry. However, if the pattern is rotated by $\pi/2$ and reflected about the mid plane, it remains unchanged [32,33]. The time series of u_r for this wavy vortex (WV) state is now time-periodic (figure 2f). Generically, time-periodic states emerge from the loss of stability of steady states via Hopf bifurcations [28,34]. However, WV states are not truly periodic solutions, but rather rotating waves [35,36]. They rotate in θ like a solid body, and as such the time-dependence disappears when integral measures such as the torque (or Nu_i) are considered (figure 2g). This is the reason why rotating waves are also known as relative equilibria [37]. In this specific example, the Hopf bifurcation is subcritical and there is hysteresis. If the flow is initialized with a WV solution at $Re_i > 150$ and then Re_i is reduced, WV remains stable down to $Re_i \approx 140$. Hence in the interval $140 \lesssim Re_i \lesssim 150$ TV and WV coexist bi-stably and both can be realized depending on the initial conditions. In addition, we found another wavy vortex solution (WV$^+$) in the same parameter range, which is stable for $Re_i \gtrsim 160$ and is characterized by a higher Nusselt number (figure 2e). Overall, these calculations exemplify the multiplicity of states common to the (supercritical) route to turbulence in TCF, which is well-known since the seminal work of Coles [17].

Further increasing the Reynolds number beyond $Re_i \approx 237$, the WV state bifurcates to a modulated wavy vortex (MWV) state [35,38]. Now, u_r becomes quasi-periodic (figure 2f) and exhibits two independent frequencies, whereas Nu_i begins to oscillate periodically with only one frequency (f_1), as is clear from the time series shown in figure 2g and the corresponding spectrum shown in figure 2h. MWV states are periodic orbits when observed from a reference frame moving at the speed of the underlying rotating wave [35] and hence are often referred to as relative periodic orbits [39]. At much larger Reynolds numbers ($Re_i \approx 1429.69$), a new independent frequency (f_2) becomes apparent in the spectrum of Nu_i (figure 2i), and the flow can be identified as a relative two-torus (R2T) [40]; i.e. a state with two independent frequencies (f_1 and f_2) when viewed in a co-moving frame. As Re_i is slightly increased (beyond $Re_i \approx 1437.50$), the R2T state breaks down into chaos, as exemplified in the (turbulent) broadband spectrum for $Re_i = 4000$ shown in figure 2k. We found other solutions in the parameter range studied here. Notably, a chaotic solution with a clearly dominant frequency (f_1) emerges (figure 2j), which is stable for a wide range of Re_i. The computed flow states illustrate the dynamical richness of the Taylor–Couette system, and indeed many other flow states may exist. Exhausting the complete set of

possible solutions (and the connections between them) is beyond the scope of this review article even for the small computational domain examined in this section.

The transition scenario observed in our simulations, including the Reynolds numbers of the instabilities, is in agreement with the experiments of Gollub & Swinney [22]. They stressed the remarkable resemblance of their experimental observations with the theory of Ruelle & Takens [23], who proved the existence of chaos close to three-frequency tori. However, as shown in figure 2*i*, the R2T state is a two-frequency tori in a co-moving reference frame. Hence, their reported breakdown is actually in better agreement with a later paper by Newhouse *et al.* [41], who proved that generic breakdown into chaos is also possible from two-tori. The resulting temporally chaotic flow initially retains spatial coherence in θ and z, but this is gradually lost as Re_i is further increased [42,43]. Nevertheless, large-scale structures called turbulent TV (because of their similarity to TV) are observed to persist in the time-averages of turbulent flows up to the highest Reynolds numbers ($Re_S = \mathcal{O}(10^6)$) investigated so far (e.g. [44]). The focus of this paper is on the transitional regime and the reader is referred to Grossmann *et al.* [45] for a review on turbulent TCF and to the recent work of Jeganathan *et al.* [46], who explore the role of Coriolis forces on the formation of turbulent Taylor rolls.

(b) Flows with defects

The results presented in the previous section were obtained using a small computational domain containing exactly one pair of TV and one azimuthal wavelength of the WV state. In the experiments [22], the WV repeated four times in θ and had eight pairs of vortices in z. This raises the question of whether the dynamics obtained in our small cell are also reproduced when spatially extended cells are considered. We carried out two DNS in a domain with $\Gamma = 25$ and spanning the whole circumference. The simulations were initialized with the corresponding CCF state disturbed with a small perturbation repeating ten times in z and four times in θ, and numerical noise in the remaining modes. At $Re_i = 200$, the CCF state rapidly destabilized and ten pairs of TV formed, which subsequently developed into a WV state of the exact same periodicity as in the simulations of the previous section. An examination of the time series of u_r and Nu_i confirmed that indeed the computed flow state is identical in both cases.

At $Re_i = 250$, these two transitions were also observed and then followed by the transition to an MVW state also exactly as in the previous section. However, after a very long time (20 viscous times units), the axial and azimuthal periodicity were lost as spatial defects appeared. A snapshot of this flow state is shown in figure 3*a*. The corresponding temporal spectrum (figure 3*b*) is continuous but features a broad, noisy peak close to the first harmonic of the spectrum of the MVW in the small domain. Similarly, all the spatial (axial) modes are excited, but as shown in figure 3*c*, the spectrum exhibits a clearly dominant peak (and harmonics) corresponding to ten pairs of vortices. Detailed investigations of transitions to chaotic flows with spatial defects, often referred to as spatio-temporal chaos (STC) [47], are scarce and deserve more attention. One example was studied in magnetohydrodynamic TCF, where the transition to defects was shown to emerge via a symmetry-breaking sub-harmonic bifurcation of a rotating wave [48]. While the temporal spectrum shown here is much noisier than that reported by Gollub & Swinney [22] for the MVW state, their spectrum also contains substantial noise. This may be due to the presence of defects in the flow, similar to those reported here, or to measurement errors, and cannot be clarified here. However, we point out that the end-walls confining the fluid in z result in distinctly different bifurcations, as demonstrated e.g. in detailed experiments [49] and in DNS [50] for systems with moderate aspect ratios ($\Gamma \sim 10$). The effect of axial end-walls is reviewed below in §3d.

(c) Flow patterns in the linearly unstable regime

The results discussed in the previous sections are specific to flows with a stationary outer cylinder ($Re_o = 0$) and that particular curvature ($\eta = 7/8$). Even for the small domain investigated in §3a,
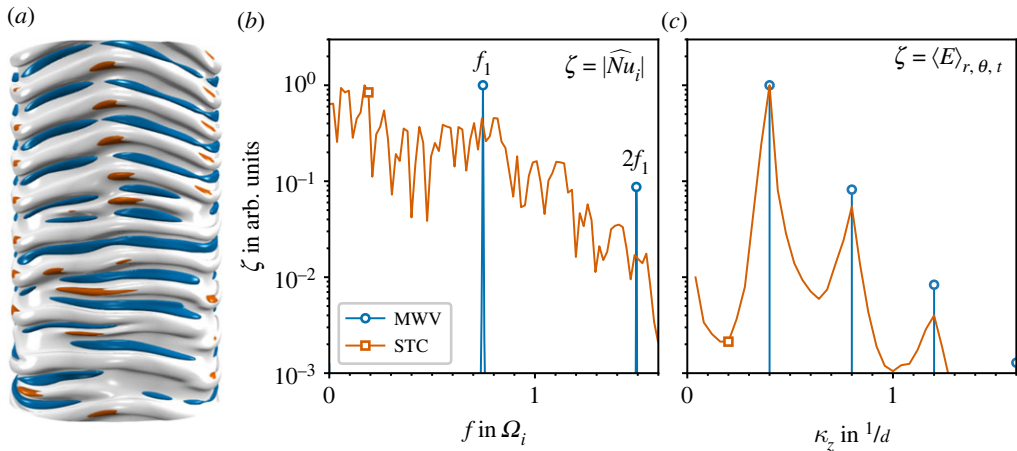
Figure 3. Onset of spatio-temporal chaos (STC) in large domains ($\Gamma = 25$, $L_\theta = 2\pi$) obtained in our simulations for fixed $\eta = 7/8$, $Re_i = 250$ and $Re_o = 0$. (*a*) Visualization of the flow state with colour-coded iso-surfaces of the velocity field (grey for $u_\theta = u_i/2$ and red/blue for $u_r = \pm u_i/20$). (*b*) Power spectra of the corresponding time series of Nu_i compared to a modulated wavy vortex (MWV) flow at the same $Re_i = 250$ but in a smaller domain with $\Gamma = 5/2$, $L_\theta = \pi/2$; i.e. the state shown in figure 2*c*. (*c*) Modal kinetic energy, $\langle E \rangle_{r,\theta,t}(\kappa_z)$, where κ_z is the axial wavenumber. (Online version in colour.)

we found coexistence of many different flow states and alternative routes to chaos (not shown in detail here). This complexity is due to the nonlinear nature of the Navier–Stokes equations, resulting in a strong dependence on the initial conditions and in typical experiments on the path in (Re_i, Re_o)-space taken to prepare the system. This was known to Coles, who in his 1965 paper [17] reported that for a given flow configuration (i.e. particular combination of Re_i and Re_o) there could be as many as 26 different possible stable flow states (characterized by their wavenumbers κ_θ and κ_z) with complicated dynamical connections between them.

When the cylinders are allowed to rotate independently in the linearly unstable region, extremely rich dynamics are found. This was beautifully illustrated by Andereck *et al.* [38], who extensively mapped out the two-dimensional parameter space spanned by (Re_i, Re_o) and revealed a large variety of flow regimes, characterized by their spatio-temporal symmetries and temporal frequencies as well as their azimuthal and axial wavenumbers. For example, in the counter-rotating regime, there exists an Re_o, at which the primary bifurcation to TV is replaced by a Hopf bifurcation to non-axisymmetric spiral vortices, which rotate in θ and travel in z. This spiral flow pattern was already observed by Taylor [1] in his seminal paper and was later studied in detail theoretically [51,52] and experimentally [53]. As the speed of the inner cylinder (Re_i) is further increased, interpenetrating spiral patterns emerge, which consist of the nonlinear superposition of spiral vortices of opposite helicity. Later the flow transitions to a chaotic state characterized by episodic bursts of turbulence superimposed on the laminar interpenetrating spirals [38,54–56]. This transition is just one of the multiple ones reported by Andereck *et al.* [38] and many others thereafter [21]. The study of the various transitions between flow states has played a central role in the development of pattern formation theory [57,58].

(d) Effect of axial end-walls

Whether comparing experimental results to the infinitely tall cylinders of theory, or to the periodic BC commonly used in simulations, the vertical boundaries of TCF are a widespread source of limitations, but also of new phenomena. Mitigating their effect started early, e.g. with Mallock [59] using a pool of mercury at the bottom of his cylinders as a buffer and Couette introducing the use of guard rings [60]. Accordingly, the results discussed so far were for experiments with relatively tall cylinders ($\Gamma \gtrsim 20$) or simulations with periodic BC. Cole [61] systematically investigated the

effect of varying Γ and observed that the critical Reynolds number for TV is in good agreement with theoretical predictions for infinitely long cylinders even for aspect ratios as low as $\Gamma = 8$. However, he also found that $\Gamma > 40$ was necessary to obtain quantitative agreement with axially periodic simulations regarding the rotation speed of the WV.

From a theoretical stand point, the presence of end-walls destroys the translation invariance of the system. In addition, the necessary discontinuity of the BC between end-walls and inner/outer cylinder generates Ekman vortices [62]. As Re_i increases, the cellular TV pattern first appears near the end-walls and then rapidly fills the entire domain, as soon as the system reaches the critical Re_i predicted for the infinite-cylinder case [61,63]. As a consequence, the transition to TV is not the result of a discrete bifurcation, but is a continuous process [63].

In systems with a stationary outer cylinder ($Re_o = 0$) and the end-walls also at rest, the end-wall boundary layers tend to flow radially inwards. However, Benjamin [63] found that cellular flows at low Γ could also have an outflow in one or both end-wall boundary layers. These flows, termed anomalous modes, are disconnected in phase space from the CCF solution and appear only at higher Re_i. For $\Gamma \approx 1$, the competition between the normal two-cell mode and the one-cell anomalous mode has been extensively investigated [64–66], along with the transition to chaos [67,68]. This specific case is particularly appealing for theoretical studies because the strong confinement drastically reduces the number of possible solutions to the Navier–Stokes equations. As Γ increases, the temporal dynamics become increasingly complex and a multitude of local [49,50] and even global [69] bifurcations have been reported.

End-wall effects have also been investigated in the counter-rotating regime, albeit less intensively. Non-axisymmetric spiral vortices can appear directly at the end-walls and propagate towards the centre of the system below the critical Reynolds number predicted by the infinite-cylinder approximation [70]. The bifurcation scenario was found to depend strongly on the end-wall rotation speed [71]. Interpenetrating spirals have also been observed in recent experiments [72] and simulations [73] for $\Gamma \approx 5$, although this small aspect ratio results in a strongly modified laminar flow and a transition scenario that is qualitatively different from that observed for tall cylinders [72].

4. Subcritical route to turbulence

The transition to turbulence in flows dominated by outer-cylinder rotation is of a completely different nature. Here, the absence of a cascade of linear instabilities starting from laminar CCF greatly complicates the transition scenario and calls for a fully nonlinear approach. First, finite-amplitude perturbations are required to destabilize the laminar flow and the mechanisms sustaining turbulence are fully nonlinear [74–76] and cannot be captured by a weakly nonlinear analysis. Second, the flow organizes itself in complex laminar–turbulent patterns, that are spatio-temporally intermittent (figure 4). As a consequence, understanding the subcritical transition in linearly stable TCF, and more generally in wall-bounded shear flows, requires stochastic approaches and additionally accounting for spatial effects. Neither of these two aspects is covered by the classical route to temporal chaos discovered by Ruelle & Takens [23] and Newhouse *et al.* [41] and discussed in the previous section. The appropriate framework to describe the onset of laminar–turbulent patterns was proposed by Kaneko [77], who extended the dynamical systems approach to linearly stable, spatially extended flows. The first experimental studies embracing his spatio-temporal perspective were carried out in the 1990s by Bottin & Chaté [14] and Bottin *et al.* [78] for PCF.

(a) Spiral turbulence and turbulent spots

For flows with stationary inner cylinder ($Re_i = 0$) and rapid outer-cylinder rotation Mallock [6] had already noted in 1896 that *when the velocity approached that at which instability was liable to occur, it was interesting to note how small a disturbance of the system was sufficient to change the entire character of the motion. A slight blow on the support which carried the apparatus, or a retardation for a few*
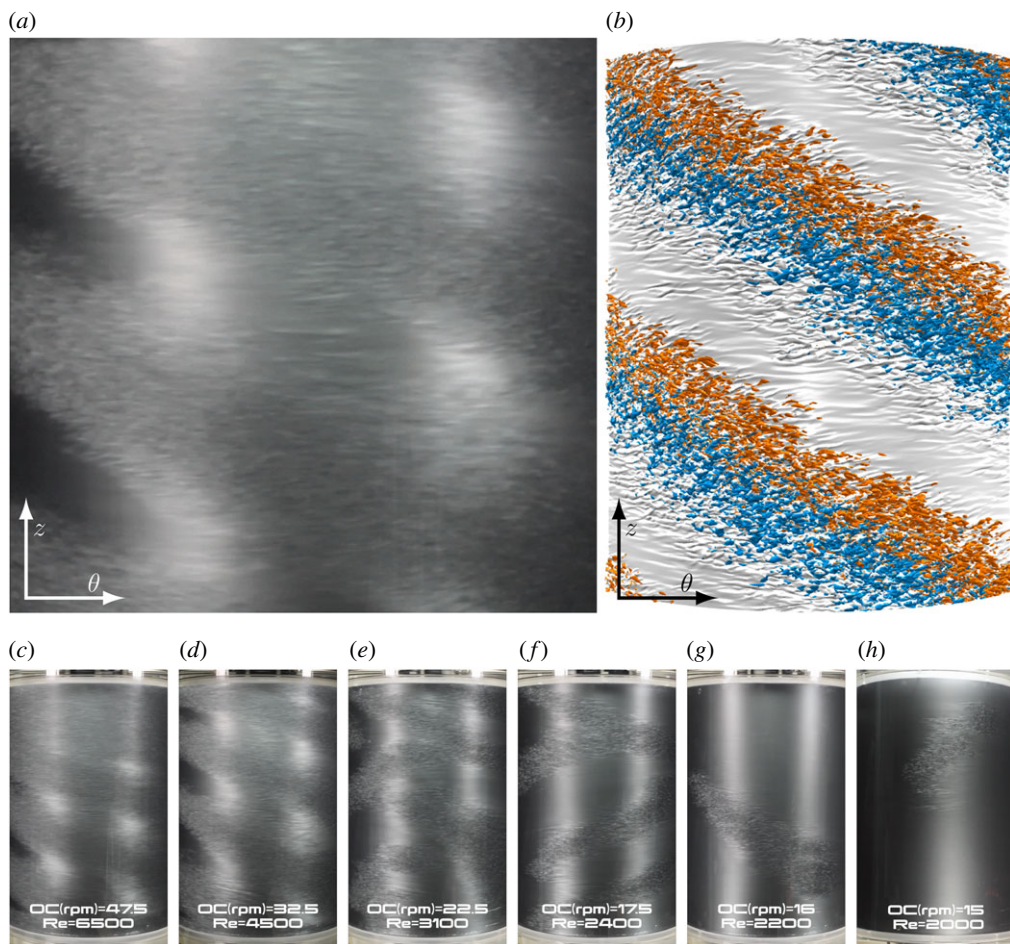
Figure 4. Spiral turbulence and turbulent spots in Taylor–Couette flow with stationary inner cylinder ($Re_i = 0$). (a) Spiral turbulence in experiments [80] for $Re_o = 4500$, $\eta = 0.97$ and $\Gamma = 92$. Kalliroscope flakes were added to the water for imaging. (b) Spiral turbulence in a direct numerical simulation for the same parameters as in (a) but for $\Gamma = 61.3$, $L_\theta = \pi/2$ and using periodic boundary conditions (BCs) in the azimuthal (θ) and axial (z) direction. Shown are colour-coded iso-contours of the velocity field ($u_\theta = u_o/2$ in grey and $u_r = \pm u_o/10$ in red/blue). (c)–(h) Sequence of flow patterns as Re_o is decreased in the experiments [80] from $Re_o = 6500$ down to 2000 (electronic supplementary material, video). (Online version in colour.)

moments of the rotation of the outer cylinder, was almost sure to produce the effect. The flow patterns emerging from this type of transition consist of well-defined turbulent domains (spots) that evolve in an otherwise laminar background, very similar to what Reynolds [3] reported for pipe flow. Coles [17] observed that individual spots sometimes spontaneously laminarized, but could also grow in size and sometimes merge with other spots. He reported that under some conditions turbulent spots came together and formed a spiral band of turbulence that cork-screwed around the apparatus (see figure 4a–d). The eminent physicist Richard Feynman, who was a Professor at Caltech at the same time as Coles, was intrigued by the origin of this surprisingly organized, but at the same time turbulent pattern, which he called *barber-pole turbulence* [79].

The emergence and death of spiral turbulence is demonstrated in figure 4c–h with snapshots from the experiments of Burin & Czarnocki [80] for $Re_i = 0$ and $\eta = 0.97$. They quasi-statically increased the rotation speed of the outer cylinder and reported an abrupt transition from laminar to spatio-temporally intermittent flow at around $Re_o \approx 4500$. Since no specific perturbations were applied to their experiments, this corresponds to the natural transition point at which ambient

noise and/or imperfections sufficed to trigger transition in their setup. Further increasing Re_o to 8000 led to a fully turbulent flow depleted of laminar regions. Subsequently, they decreased Re_o to study the spatio-temporal dynamics of turbulence. The snapshots in figure 4c–h, and the corresponding electronic supplementary material, movie, illustrate how laminar regions gradually appear and grow in size as Re_o is reduced, leading to the formation of laminar–turbulent spiral patterns. This transition process from fully turbulent TCF to laminar–turbulent spiral patterns can be understood as a spatial modulation of the fully turbulent state [81], arising from a linear instability of the latter [82]. As Re_o was further decreased, the spiral turbulence retained its form, until it began to progressively disintegrate into spots. These spots were sometimes elongated, in line with the spiral angle, and their boundary appeared to propagate in this direction as well (see e.g. the video at $Re_o = 2100$). Finally, the flow laminarized fully at $Re_o \approx 2000$. We stress that the parameter regime $Re_o \in [2000, 4500]$ is characterized by strong hysteresis. Here, the history of the flow (i.e. its path taken in parameter space) determines the observed flow state for a given Re_o. If the flow is initially laminar and 'undisturbed', it remains laminar forever. By contrast, if it is initially turbulent (or laminar, but sufficiently disturbed), it remains turbulent.

This behaviour is not specific to flows with a stationary inner cylinder, but extends to most of the counter-rotating regime of TCF [38,55,56]. Figure 5a shows the regime diagram for $\eta = 0.98$. We first focus on the transition scenario for $Re_o = -1000$, which was the focus of an experimental study by Avila & Hof [56]. As Re_i exceeds 650, the laminar flow becomes unstable to a spiral mode and accordingly a transition to interpenetrating laminar spiral patterns was observed in the experiments. Upon a slight increase in Re_i turbulent spots spontaneously formed and decayed in an unpredictable manner, while the interpenetrating spirals remained largely unaffected in the background, as exemplarily shown figure 5b. This intriguing flow state was discussed briefly in §3c and has been reported by many authors [38,54–56]. Avila & Hof [56] then reduced Re_i and noted that the interpenetrating spirals vanished, while the turbulent spots organized themselves into turbulent spiral arms interspersed in the remaining laminar background (figure 5c). The resulting spiral turbulence remained robust as Re_i was further reduced, until it disintegrated into spots and ultimately laminarized fully at $Re_i = 525$. Similar results were obtained for other Re_o. As shown in figure 5a, the faster the rotation of the outer cylinder, the larger the region of hysteresis in which spiral turbulence or fully laminar flow can be observed (depending on the initial conditions). For the same geometry, Prigent et al. [83] did not detect hysteresis. In their experiments, the natural transition point coincides approximately with the laminarization border of spiral turbulence. This suggests a high level of background disturbance in their setup and illustrates the dependence of the natural transition point on technical details of the apparatus. Overall, the results of Avila & Hof [56] are in qualitative agreement with earlier numerical simulations of Meseguer et al. [55], who studied the counter-rotating regime for $\eta = 0.883$ in detail.

We remark that in the experiments of Burin & Czarnocki [80] and Avila & Hof [56] the subcritical turbulence was created differently. In the latter, the laminar flow reproducibly became unstable as Re_i was increased above the linear instability threshold. By successively decreasing Re_i below this threshold, the subcritical turbulence was investigated. By contrast, in the experiments of Burin & Czarnocki [80] with a stationary inner cylinder, a linear instability was unavailable and finite-amplitude disturbances (e.g. unavoidable imperfections in the setup, vibrations or ambient noise) trigger turbulence, as in Prigent's setup [83]. Despite this difference, the reverse transition from turbulent to laminar flow, as the Reynolds number decreases, is less sensitive to disturbances. Generally, in the subcritical regime, the properties of the laminar–turbulent patterns are intrinsic to the system and independent of how the turbulent flow is initialized.

The lower boundary for the laminarization of turbulent spots has been measured by many authors experimentally [14,15,17,38,55,56,80,85] and in DNS [55,86,87]. These measurements are summarized in figure 6, where the lowest Re_S for turbulence survival is shown as a function of R_Ω. Recall that $R_\Omega = 0$ corresponds to exact counter-rotation and the first data point (lowest R_Ω) here corresponds to PCF flow with $Re_S \approx 1300$ [14], which we calculated as $Re_S = 4Re$, where
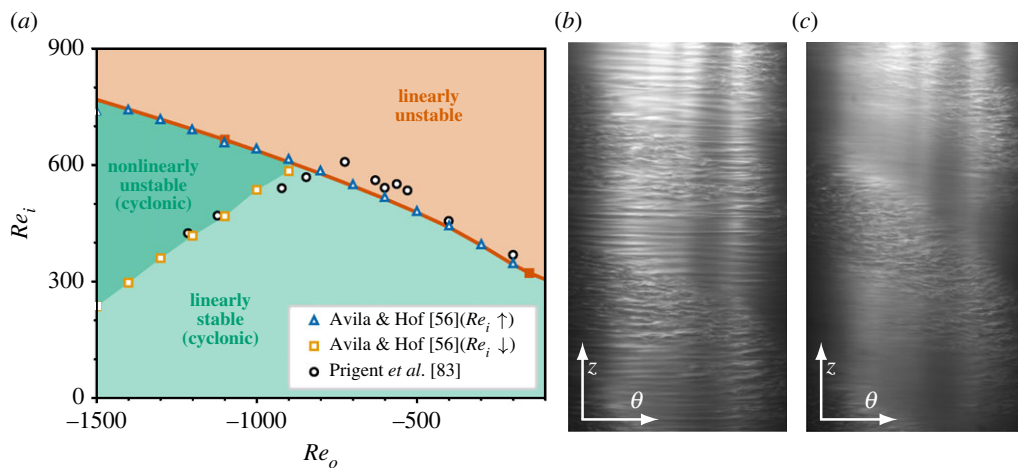
Figure 5. Sub- and supercritical spiral turbulence in Taylor–Couette flow experiments [56,83], both with counter-rotating cylinders and narrow gaps ($\eta \approx 0.98$). (*a*) Laminar flow can exist everywhere below the theoretical neutral stability curve (red line with full squares as in figure 1). In the linearly stable cyclonic regime (light green) it is the only flow state. In the nonlinearly unstable hysteretic regime (dark green) laminar flow or subcritical spiral turbulence can be observed, depending on the flow history and the existence of finite-amplitude perturbations. Above the neutral stability curve, laminar interpenetrating spirals arise, sometimes coexisting with turbulent spots/spirals. (*b*) Supercritical spiral turbulence featuring intermittent turbulent spirals on top of laminar interpenetrating spirals [84]. (*c*) Subcritical spiral turbulence with the typical coexisting laminar and turbulent domains [84]. (Online version in colour.)

Re is the Reynolds number commonly defined for PCF. This is followed by the experiments of Klotz *et al.* [15] for an extremely narrow gap ($\eta = 0.997$) and stationary inner cylinder with $Re_S \approx 1320$ and $R_\Omega = 0.003$. As R_Ω is increased and cyclonic rotation is added, higher Re_S are required to sustain turbulence. As shown in figure 6, experimental data from various studies collapse well into a single curve despite the wide ranges covered in curvature ($\eta \in [0.789, 1]$) and in Reynolds numbers ($Re_i \in [-1000, 1200]$ and $Re_o \in [-50000, -1200]$). One exception to this are the transition points obtained by Burin & Czarnocki [80] for wide gaps, $\eta = 0.73$ and 0.55 (the latter not shown in the plot, as it corresponds to much larger R_Ω). For a fixed experimental apparatus, wider gaps result in lower Γ. In combination with the increased Re_S, which is required for subcritical transition, this leads to end-wall effects becoming very significant for the laminarization boundary. In that case, the end-walls greatly perturb the laminar base state and may trigger subcritical transition [80] or even result in linear instabilities [90–92]. For channel flow, it has been recently shown that end-walls destabilize laminar–turbulent bands and can cause relaminarization [93,94].

The remarkable collapse of the data (figure 6) illustrates the suitability of the parametrization introduced by Dubrulle *et al.* [19] and demonstrates that the specific case of stationary inner cylinder (i.e. $R_\Omega = (1/\eta) - 1$) does not exhibit some form of singularity, as figure 1*a* may initially suggest. This point is further confirmed by the experiments of Coles [17], who continued the laminarization curve from the counter-rotating to the co-rotating regime. Note also that curvature appears to influence the laminarization boundary only indirectly through R_Ω, at least for $\eta \gtrsim 0.789$.

Extending measurements to larger R_Ω would be valuable, but is challenging. Specifically, as R_Ω increases, Re_S grows exponentially, necessarily resulting in a huge difference between the angular speeds of the inner and outer cylinders. This exacerbates end-wall effects in experiments and has extremely high computational cost in axially periodic DNS. Finally, we stress that the boundary at which turbulence can become sustained depends only on the system parameters. By contrast, the natural (uncontrolled) transition boundary, where turbulence is observed to appear
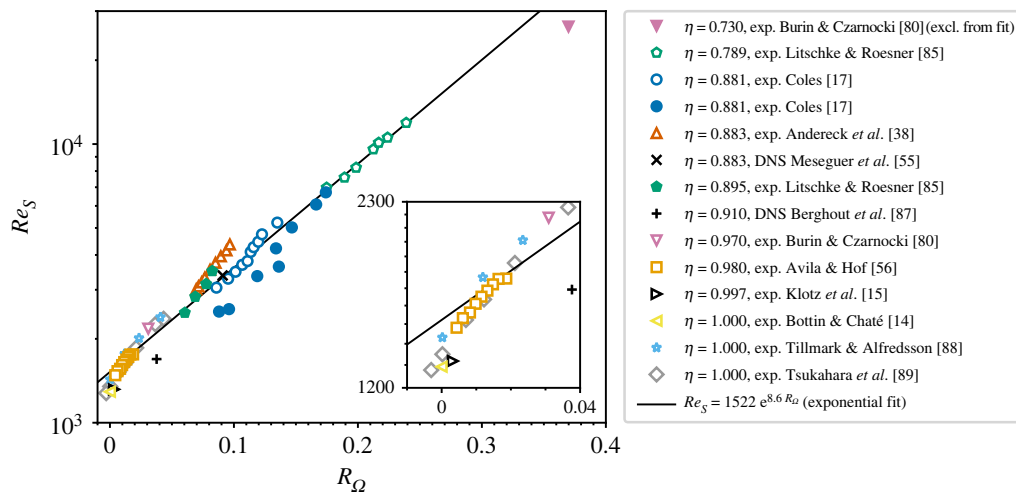
Figure 6. Laminarization boundary of turbulent spots in terms of the critical shear Reynolds number (Re_S) as a function of the rotation number (R_Ω). The datasets from many different experiments [14,15,17,38,56,80,85,88,89] and simulations [55,87] span a wide range of curvatures ($\eta \in [0.73, 1)$) and Reynolds numbers ($Re_i \in [-1000, 1200]$, $Re_o \in [-50\,000, -1200]$). Most measurements were taken in the subcritical counter-rotating regime or for stationary inner cylinder, but Coles [17] also performed measurements in the co-rotating cyclonic regime. Note that in typical experimental setups with fixed cylinder length, an increase in gap width (i.e. a decrease in η) comes at the price of a decrease in Γ. As a consequence, the critical Re_S is more affected by the specific end-cap configuration. Thus, the data of Burin & Czarnocki [80] for wide gaps ($\eta = 0.73$ and $\eta = 0.55$, the latter not shown here) were excluded from the exponential fit. (Online version in colour.)

as Re_S is increased, depends on the level of disturbance present in the experiment and can vary by as much as one order of magnitude in Re_S for the same geometry and a fixed value of R_Ω [16].

(b) Transient turbulence: stochastic decay of turbulent spots

The experiments reported by Mallock [6], Taylor [11] and Coles [17] demonstrated that, once triggered, turbulent episodes can last almost indefinitely or relaminarize after irregular intervals. This essentially implies that the lower boundary discussed in the previous section depends on the observation time and on the experimental realization, which in part explains the scatter in figure 6.

The first systematic study of the stochastic nature of turbulence decay in TCF was performed in 2010 by Borrero-Echeverry et al. [95]. They investigated a system driven by pure outer-cylinder rotation ($Re_i = 0$) and repeated the experiments up to 1200 times for every Re_o in order to statistically characterize the duration of turbulent episodes. Their flow visualizations indicated that turbulence collapses suddenly and without warning. The duration (or lifetime) t_{turb} of turbulence at $Re_o = 8106$ in each experimental run is shown in figure 7a. The corresponding lifetime distribution, shown in figure 7b, is approximately exponential. This implies that relaminarization follows a memoryless process, exactly as reported earlier for plane Couette [14] and pipe [96,97] flows. By collecting lifetime distributions at various Re_o, Borrero-Echeverry et al. [95] showed that the associated time constant τ_d (i.e. the average lifetime) increases super-exponentially with Re_o, but remains finite as Re_o increases. This result, in qualitative agreement with previous studies of pipe flow [98,99], was confirmed by Alidai et al. [100], who additionally showed that τ_d does not depend on the specific details of how the turbulence is initially triggered, but is significantly affected by imperfections in the experimental apparatus, and by the end-wall conditions. Finally, they also showed that as Γ is reduced, τ_d decreases.

Goldenfeld et al. [101] proposed that turbulent spots relaminarize when all turbulent fluctuations within the spot fall below a certain level. With this assumption they exploited
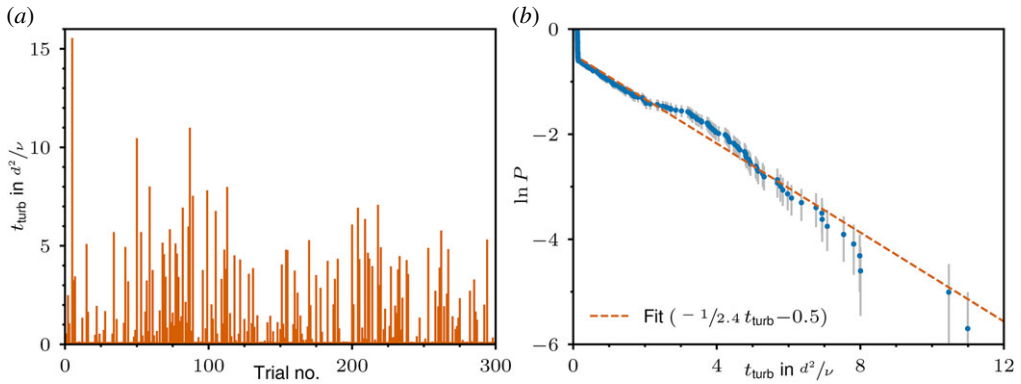
Figure 7. Lifetime statistics of turbulent episodes in Taylor–Couette flow experiments [95] at $Re_i = 0$, $Re_o = 8106$, $\eta = 0.871$ and $\Gamma = 33.6$. (a) Duration (t_{turb}) of turbulent episodes after triggering turbulence by briefly counter-rotating the inner cylinder in 300 experimental realizations. For some runs turbulence collapses almost immediately, but for others it persists up to $\mathcal{O}(10^1)$ viscous time units (d^2/ν), which for this Reynolds number corresponds to $\mathcal{O}(10^5)$ convective time units (d/u_o). (b) Probability (P) that turbulence survives up to time t_{turb}. The runs where turbulence collapses immediately ($t_{turb} \approx 0$), are highlighted by an almost vertical drop in P. For the rest of the runs, P decays approximately exponentially, as indicated by the linear fit (broken line) with the slope $-1/\tau_d$. Here, $\tau_d \approx 2.4$ is the average survival time. Note the semi-log scale of the plot. The error bars (grey) represent the sampling error. (Online version in colour.)

extreme-value theory, where super-exponential scaling appears as a matter of course [102], to develop a model consistent with the scaling of τ_d observed in experiments [95,98]. This idea has recently been validated and elaborated further in DNS studies [103,104].

(c) Onset of sustained turbulence: spatio-temporal proliferation of spots

Despite the transient nature of individual turbulent spots, Moxey & Barkley [105] showed a mechanism by which the proliferation of turbulent spots (i.e. puffs in their case) can lead to sustained turbulence in pipe flow. Avila *et al.* [106] further showed that the probability of a puff to grow and shed a daughter one, statistically identical to its parent, increases as the Reynolds number increases. Specifically, the associated proliferation time constant decreases super-exponentially with Reynolds number. The competition between the stochastic processes of turbulence decay and turbulence proliferation determines the critical Reynolds number for the onset of sustained turbulence in pipe flow [106]. The same mechanism was later demonstrated in a narrow-gap Taylor–Couette system [107], in which the computational domain was spatially extended in one direction only (as happens naturally in pipe flow).

Beyond the critical point, turbulence proliferates faster than it decays and the fraction of the flow domain occupied by turbulence increases with Reynolds number. This was explicitly demonstrated by Lemoult *et al.* [108], who precisely measured the evolution of the turbulence fraction as a function of Re_o for a system with stationary inner cylinder and a very narrow gap ($\eta = 0.998$). The short aspect ratio they used ($\Gamma = 8$) allowed turbulence to localize only in θ, while filling the apparatus in z completely. The turbulence fraction was found to increase continuously from zero at the critical point, corresponding to a second-order phase transition. The spatio-temporal dynamics of the turbulent spots, and of the laminar gaps between them, could be shown to fall into the universality class of directed percolation (DP), which is the simplest case of a non-equilibrium phase transition. We stress that in this system the dynamics of spots is exactly as in pipe flow due to the axial confinement. The critical exponents could be accurately determined with extremely long measurement times, because TCF is a closed system in contrast to pipe flow, where turbulent puffs ultimately leave the pipe at its downstream end.

It is worth noting that the mechanisms of turbulent proliferation are qualitatively different in flows extended in one and in two directions. In the former, the turbulence fraction can only increase as the spots grow in the azimuthal direction (θ), whereas in the latter, spots can also extend in the axial direction (z). In both cases the transition is of second order [84]. Moreover, recent measurements by Klotz et al. [15] in very tall cylinders ($\Gamma = 750$) with a very narrow gap ($\eta = 0.997$) exhibit also a DP transition; but with exponents characteristic of systems extended in two directions (here in θ and z). The interested reader is referred to two recent reviews about laminar–turbulent patterns in wall-bounded flows extended in two spatial directions [109] and about the role of DP for turbulence transition in general [110].

(d) Simple invariant solutions and the origin of transient turbulence

The results discussed in the previous section resolve the question of the onset of sustained turbulence in linearly stable flows, but do not provide information as to how chaotic dynamics appears in the phase space of the system. In an influential paper, Nagata [111] showed in 1990 that a specific WV solution, similar to the WV shown in figure 2b for stationary outer cylinder, could be numerically continued from Taylor–Couette to plane Couette flow (without rotation). In this limit, Nagata's WV solution remains three-dimensional, but becomes steady. More importantly, it is disconnected from the laminar (plane) Couette flow in phase space, a result that holds already for TCF in very narrow gaps ($\eta \gtrsim 0.993$) [20]. In other words, in PCF there is no sequence of instabilities leading from its laminar base state to WV flow, because the base state is linearly stable. Nagata's discovery paved the way for applying the dynamical systems approach to linearly stable flows.

At the lowest Reynolds number (called saddle-point) at which Nagata's WV solution exists, it is stable in a certain symmetry-restricted subspace (but unstable in full space). As shown in figure 8 (data re-plotted with permission from Kreilos & Eckhardt [112]), at Reynolds numbers slightly above the saddle-point this solution undergoes a Hopf bifurcation leading to a periodic solution [113]. This is exactly like the bifurcation from a WV state into a relative periodic solution (MWV) shown earlier in figure 2e for TCF. As Re_S is further increased, a period-doubling cascade (PDC) renders the flow chaotic. Despite the difference in the precise bifurcations occurring here in PCF and in the case of TCF, the situation is similar in both cases. Chaos emerges from a simple solution (WV) after a short bifurcation sequence during which symmetries are lost and the temporal complexity increases. We, however, stress that in PCF, these changes in phase space occur far away from the laminar base state, which actually remains stable to infinitesimal disturbances for arbitrarily large Reynolds numbers [114].

As Re_S is further increased, the chaotic attractor's volume grows in phase space, i.e. larger fluctuations of the velocity occur. Finally, the attractor collides with a twin lower branch WV solution, born at the same saddle-node bifurcation, and is destroyed [115,116]. Beyond this Re_S the chaotic dynamics is not sustained, but transient, and the resulting lifetime distributions are exponential [117]. Although this is consistent with the experimental observations at larger Re_S described in the previous section, there are crucial qualitative differences. The DNS described in this section were performed by imposing artificial symmetries in small computational cells. This stabilizes the solutions, simplifies the temporal dynamics and precludes the spatial localization typical of turbulent spots. In conclusion, a wide gap between theory and experiment remains at this stage. The interested reader is referred to the recent review by Avila et al. [9] with main focus on pipe flow.

Several families of simple solutions with distinct symmetries have been computed in TCF to date [118–120]. A particularly interesting solution computed for PCF [121] is spatially localized in the form of a spiral, similar to the spiral turbulence observed in experiments and shown in figure 4. Generally, these solutions are all unstable, but it has been demonstrated that the phase space of the turbulent dynamics is organized around them and their stable and unstable manifolds [122,123]; reviews are given by Graham & Floryan [124] and Kawahara et al. [125]. More
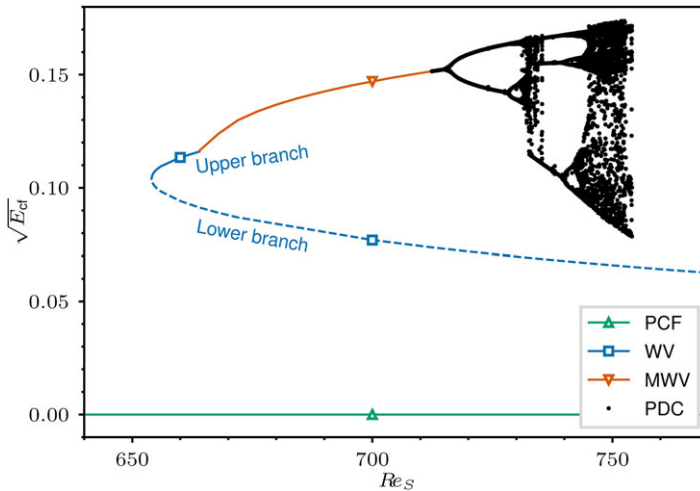
Figure 8. Bifurcation diagram showing the onset of chaotic transients in plane Couette flow (PCF) in a small, symmetry-restricted cell. The kinetic energy contained in the cross-flow velocity components, $\sqrt{E_{cf}}$, is shown as a function of the shear Reynolds number (Re_S). A pair of steady wavy vortex (WV) solutions is born at a saddle-node bifurcation at $Re_S \approx 655$. The upper branch is stable in the symmetry-restricted space, but loses stability in a Hopf bifurcation to a modulated wavy vortex (MWV) state at $Re_S \approx 664$. Subsequently, a period-doubling cascade (PDC) generates a chaotic attractor, although there is a short window ($735 < Re_S < 740$) with a stable period three state. The chaotic attractor is destroyed at $Re_S \approx 754$ and thereafter all trajectories laminarize. Note that the shear Reynolds number is related to the usual plane Couette Reynolds number as $Re_S = 4Re$. The data shown in this figure is re-plotted with permission from Kreilos & Eckhardt [112]. (Online version in colour.)

recent studies using a Taylor–Couette system with $\Gamma = 1$ have provided experimental evidence supporting the importance of simple solutions in organizing the turbulent dynamics [126–128].

We conclude this section by noting that Deguchi [129] recently made the surprising discovery of a linear instability of TCF with stationary inner cylinder. However, for typical experimental gap widths (i.e. $\eta \gtrsim 0.1$), this instability only occurs for $Re_o \gtrsim 10^7$. Even if these extreme Reynolds numbers could be attained in experiments (not achieved so far), subcritical transition would certainly occur well before this instability could be observed.

5. Quasi-Keplerian regime

Because of its potential relevance to astrophysical flows, the QK regime of TCF ($-\infty < R_\Omega < -1$, blue region in figure 1) has attracted particular interest in recent years. A thin disc of gas in orbital motion around a central gravitating body is a paradigmatic scenario in astronomy usually associated with the beginning or end of stellar lifetime [130–132]. In principle, accretion in astrophysical discs requires a radial transport of orbiting gas towards the central mass, and the corresponding inward loss of angular momentum is explained by an outward transport of the same. If the orbiting motion is laminar, the only mechanism available to maintain outward momentum transport is molecular viscosity, which is orders of magnitude too low for accretion to take place on the inferred time scales. Thus the transport is naturally turbulent, but the possible origin of this turbulence has generated considerable discussion.

In astrophysical discs, the angular velocity of the orbiting gas is often assumed to scale as $\Omega \propto r^{-q}$, where r is the distance to the central object and $q = -2/R_\Omega$ fully characterizes the flow with $q = 3/2$ corresponding to Keplerian flow ($R_\Omega = -4/3$) [19]. Significantly, the flow in the QK regime is linearly stable according to the Rayleigh criterion. While magnetic fields can drive turbulence via magnetorotational instabilities [133], it remains unclear whether such instabilities operate in cooler (i.e. weakly ionized) discs, where the gas is largely neutral and the ambient magnetism may not play a significant dynamical role. For ordinary (non-conducting) homogeneous fluids,

any transition in the QK regime is expected to be subcritical. It is, however, noted that results from cyclonic subcritical flows, discussed in the previous section, do not offer much guidance for the anti-cyclonic QK regime.

For almost two decades, experiments in the QK regime presented conflicting results. Ji *et al.* [134], used laser Doppler velocimetry (LDV) to demonstrate that a quiescent flow is maintained even up to $Re_S = 2 \times 10^6$, which was at the limit of their experimental apparatus. They then surmised by extrapolation that discs were hydrodynamically stable. However, the opposite conclusion was reached by Paoletti & Lathrop [135] for slightly lower Re_S, using torque measurements as an integral measure of the angular momentum transport. In both experiments considerable care was taken to minimize end-wall effects. While Ji *et al.* [134] used split, independently-rotating end-caps, Paoletti & Lathrop [135] measured the torque only on a central portion of the inner cylinder.

The influence of end-wall effects has remained an epicentre of discussion and disagreement, but the problem has come into better focus more recently. First, further experiments [136], where a high-Re_S QK flow was actively perturbed, demonstrated robust stability (i.e. laminar flow at high Re_S), bolstering the earlier result [134]. Second, DNS [91,137] brought significant clarity to the apparently conflicting experimental results in detailing how boundary effects can be significant even at moderate Re_S. Specifically, if the end-wall conditions are carefully chosen, turbulence becomes confined to thin boundary layers as Re_S increases, while the bulk flow remains laminar [137]. This result is consistent with axially periodic DNS [138,139] and with radially resolved observations in cyclonic experiments [80] and thus points to a general care needed when interpreting results. For additional elaboration on the QK regime and related topics we refer the reader to the papers by Ji & Goodman [140] and by Guseva & Tobias [141].

6. Conclusion

Starting with Taylor's groundbreaking work, Taylor–Couette flow has become the archetype to study hydrodynamic stability, bifurcations, pattern formation, transition to turbulence and highly turbulent wall-bounded flows. More generally, the development of the dynamical systems framework to study dissipative systems has been greatly inspired and influenced by experimental observations of this very system. The detailed bifurcation mechanisms and features of the flow patterns depend sensitively on the four dimensionless control parameters of the problem (Re_i, Re_o, η, Γ) and on the axial BCs. As a consequence, the dynamical richness of TCF has no limits and in this review we have only summarized briefly some of the main traits.

Despite qualitative differences in the instabilities and flow patterns preceding turbulence, the transition to turbulence falls into one of two main categories, which we termed supercritical and subcritical. The first one is characterized by a sequence of bifurcations eventually leading to temporally chaotic dynamics. The ensuing flow patterns fill the whole apparatus and sequentially lose spatial symmetry and coherence. These bifurcations were studied experimentally, numerically and theoretically in great detail in the last century. The catastrophic, subcritical route to turbulence was also studied and characterized experimentally back then, but it is only in the last two decades that an understanding of the underlying mechanisms has emerged. This has been possible thanks to statistically resolved spatio-temporal characterizations of very large systems up to extremely long observation times. The two key physical mechanisms underlying the DP transition to sustained turbulence in linearly stable TCF are turbulence decay and proliferation. Both are stochastic processes. In the counter-rotating regime, things become even more complicated as the linearly unstable layer close to the inner cylinder interacts with the linearly stable (but nonlinearly unstable) one close to the outer cylinder. This results in a mixture of the two transition routes and is a topic that deserves more attention. It is not only relevant to TCF, but also to e.g. curved pipes [142].

A third, perhaps even more intriguing case is the absence of turbulence and hence of a route to it in the QK regime. Here, the weight of the experimental evidence suggests that CCF is nonlinearly stable up to at least $Re_S = \mathcal{O}(10^6)$. Whether transition occurs at even higher

Reynolds numbers remains an outstanding question. The exponential stabilization of CCF with increasing R_Ω in the cyclonic regime revealed in this review cannot be extrapolated to the anti-cyclonic regime, but highlights the efficiency of the Coriolis force in undermining the regeneration mechanisms of wall-bounded turbulent flows.

References

1. Taylor GI. 1923 VIII. Stability of a viscous liquid contained between two rotating cylinders. *Phil. Trans. R. Soc. Lond. A* **223**, 289–343. (doi:10.1098/rsta.1923.0008)
2. Eckert M. 2010 The troublesome birth of hydrodynamic stability theory: sommerfeld and the turbulence problem. *Eur. Phys. J. H* **35**, 29–51. (doi:10.1140/epjh/e2010-00003-3)
3. Reynolds O. 1883 An experimental investigation of the circumstances which determine whether the motion of water shall be direct or sinuous, and of the law of resistance in parallel channels. *Phil. Trans. R. Soc.* **174**, 935–982. (doi:10.1098/rstl.1883.0029)
4. Orr WM. 1907 The stability or instability of the steady motions of a perfect liquid and of a viscous liquid. Part II: a viscous liquid. *Proc. R. Irish Acad. Sect. A: Math. Phys. Sci.* **27**, 69–138.
5. Sommerfeld A. 1909 Ein Beitrag zur hydrodynamischen Erklärung der turbulenten Flüssigkeitsbewegung. In *Proc. of the 4th Int. Mathematical Congress*, Rome, Italy, 1908, vol. 3, pp. 116–124. Tipografia della R. Accademia dei Lincei.
6. Mallock A. 1896 Experiments on fluid viscosity. *Phil. Trans. R. Soc. Lond. A* **1897**, 41–56. (doi:10.1098/rsta.1896.0003)
7. Lord Rayleigh. 1917 On the dynamics of revolving fluids. *Phil. Trans. R. Soc. Lond. A* **93**, 148–154. (doi:10.1098/rspa.1917.0010)
8. Couette M. 1890 Distinction de deux régimes dans le mouvement des fluides. *J. Phys. Théor. Appl.* **9**, 414–424. (doi:10.1051/jphystap:018900090041401)
9. Avila M, Barkley D, Hof B. 2023 Transition to turbulence in pipe flow. *Annu. Rev. Fluid Mech.* **55**, 575–602. (doi:10.1146/annurev-fluid-120720-025957)
10. Wendt F. 1933 Turbulente Strömungen zwischen zwei rotierenden konaxialen Zylindern. *Ingenieur-Archiv* **4**, 577–595. (doi:10.1007/BF02084936)
11. Taylor GI. 1936 Fluid friction between rotating cylinders I – torque measurements. *Proc. R. Soc. Lond. A* **157**, 546–564. (doi:10.1098/rspa.1936.0215)
12. Barkley D. 2016 Theoretical perspective on the route to turbulence in a pipe. *J. Fluid Mech.* **803**, P1. (doi:10.1017/jfm.2016.465)
13. Daviaud F, Hegseth J, Bergé P. 1992 Subcritical transition to turbulence in plane Couette flow. *Phys. Rev. Lett.* **69**, 2511–2514. (doi:10.1103/PhysRevLett.69.2511)
14. Bottin S, Chaté H. 1998 Statistical analysis of the transition to turbulence in plane Couette flow. *Eur. Phys. J. B* **6**, 143–155. (doi:10.1007/s100510050536)
15. Klotz L, Lemoult G, Avila K, Hof B. 2022 Phase transition to turbulence in spatially extended shear flows. *Phys. Rev. Lett.* **128**, 014502. (doi:10.1103/PhysRevLett.128.014502)

16. Schultz-Grunow F. 1959 Zur Stabilität der Couette-Strömung. *Z. Angew. Math. Mech.* **39**, 101–110. (doi:10.1002/zamm.19590390303)

17. Coles D. 1965 Transition in circular Couette flow. *J. Fluid Mech.* **21**, 385–425. (doi:10.1017/S0022112065000241)

18. Maretzke S, Hof B, Avila M. 2014 Transient growth in linearly stable Taylor–Couette flows. *J. Fluid Mech.* **742**, 254–290. (doi:10.1017/jfm.2014.12)

19. Dubrulle B, Dauchot O, Daviaud F, Longaretti P, Richard D, Zahn J. 2005 Stability and turbulent transport in Taylor–Couette flow from analysis of experimental data. *Phys. Fluids* **17**, 095103. (doi:10.1063/1.2008999)

20. Faisst H, Eckhardt B. 2000 Transition from the Couette–Taylor system to the plane Couette system. *Phys. Rev. E* **61**, 7227–7230. (doi:10.1103/PhysRevE.61.7227)

21. Tagg R. 1994 The Couette–Taylor problem. *Nonlinear Sci. Today* **4**, 1–25.

22. Gollub JP, Swinney HL. 1975 Onset of turbulence in a rotating fluid. *Phys. Rev. Lett.* **35**, 927. (doi:10.1103/PhysRevLett.35.927)

23. Ruelle D, Takens F. 1971 On the nature of turbulence. *Commun. Math. Phys.* **20**, 167–192. (doi:10.1007/BF01646553)

24. López JM, Feldmann D, Rampp M, Vela-Martín A, Shi L, Avila M. 2020 nsCouette–a high-performance code for direct numerical simulations of turbulent Taylor–Couette flow. *SoftwareX* **11**, 100395. (doi:10.1016/j.softx.2019.100395)

25. Ostilla-Mónico R, Verzicco R, Grossmann S, Lohse D. 2016 The near-wall region of highly turbulent Taylor–Couette flow. *J. Fluid Mech.* **788**, 95–117. (doi:10.1017/jfm.2015.675)

26. Feldmann D, Morón D, Avila M. 2021 Spatiotemporal intermittency in pulsatile pipe flow. *Entropy* **23**, 1–19. (doi:10.3390/e23010046)

27. Hopf E. 1948 A mathematical example displaying features of turbulence. *Commun. Pure Appl. Math.* **1**, 303–322. (doi:10.1002/cpa.3160010401)

28. Kuznetsov YA 2004 *Elements of applied bifurcation theory*, 3rd edn. Applied Mathematical Sciences Series. New-York, NY: Springer–Verlag.

29. Chossat P, Lauterbach R. 2000 *Methods in equivariant bifurcations and dynamical systems*. Singapore: World Scientific.

30. Chossat P, Iooss G. 1994 *The Couette–Taylor problem*. Berlin, Germany: Springer–Verlag.

31. Crawford JD, Knobloch E. 1991 Symmetry and symmetry-breaking bifurcations in fluid dynamics. *Annu. Rev. Fluid Mech.* **23**, 341–387. (doi:10.1146/annurev.fl.23.010191.002013)

32. Marcus PS. 1984 Simulation of Taylor–Couette flow. Part 2. Numerical results for wavy-vortex flow with one travelling wave. *J. Fluid Mech.* **146**, 65–113. (doi:10.1017/S0022112084001774)

33. Wereley ST, Lueptow RM. 1998 Spatio-temporal character of non-wavy and wavy Taylor–Couette flow. *J. Fluid Mech.* **364**, 59–80. (doi:10.1017/S0022112098008969)

34. Hopf E. 1942 Abzweigung einer periodischen Lösung von einer stationären Lösung eines Differentialsystems. *Ber. Math.-Phys. Kl Sächs. Akad. Wiss. Leipzig* **94**, 1–22.

35. Rand D. 1982 Dynamics and symmetry. Predictions for modulated waves in rotating fluids. *Arch. Ration. Mech. Anal.* **79**, 1–37. (doi:10.1007/BF02416564)

36. King GP, Li Y, Lee W, Swinney HL, Marcus PS. 1984 Wave speeds in wavy Taylor-vortex flow. *J. Fluid Mech.* **141**, 365–390. (doi:10.1017/S0022112084000896)

37. Krupa M. 1990 Bifurcations of relative equilibria. *SIAM J. Math. Anal.* **21**, 1453–1486. (doi:10.1137/0521081)

38. Andereck CD, Liu SS, Swinney HL. 1986 Flow regimes in a circular Couette system with independently rotating cylinders. *J. Fluid Mech.* **164**, 155–183. (doi:10.1017/S0022112086002513)

39. Viswanath D. 2007 Recurrent motions within plane Couette turbulence. *J. Fluid Mech.* **580**, 339–358. (doi:10.1017/S0022112007005459)

40. Wulff C, Lamb JSW, Melbourne I. 2001 Bifurcation from relative periodic solutions. *Ergod. Theory Dyn. Syst.* **21**, 605–635. (doi:10.1017/S0143385701001298)

41. Newhouse S, Ruelle D, Takens F. 1978 Occurrence of strange axiom *A* attractors near quasi periodic flows on T^m, $m \geq 3$. *Commun. Math. Phys.* **64**, 35–40. (doi:10.1007/BF01940759)

42. Brandstäter A, Swinney HL. 1987 Strange attractors in weakly turbulent Couette–Taylor flow. *Phys. Rev. A* **35**, 2207–2220. (doi:10.1103/PhysRevA.35.2207)

43. Lathrop DP, Fineberg J, Swinney HL. 1992 Transition to shear-driven turbulence in Couette–Taylor flow. *Phys. Rev. A* **46**, 6390–6405. (doi:10.1103/PhysRevA.46.6390)

44. Huisman SG, Van Der Veen RC, Sun C, Lohse D. 2014 Multiple states in highly turbulent Taylor–Couette flow. *Nat. Commun.* **5**, 1–5. (doi:10.1038/ncomms4820)

45. Grossmann S, Lohse D, Sun C. 2016 High-Reynolds number Taylor–Couette turbulence. *Annu. Rev. Fluid Mech.* **48**, 53–80. (doi:10.1146/annurev-fluid-122414-034353)

46. Jeganathan V, Alba K, Mónico RO. 2023 Exploring the origin of turbulent Taylor rolls. *Phil. Trans. R. Soc. A* **381**, 20220130. (doi:10.1098/rsta.2022.0130)

47. Cross M, Hohenberg P. 1994 Spatiotemporal chaos. *Science* **263**, 1569–1570. (doi:10.1126/science.263.5153.1569)

48. Guseva A, Willis A, Hollerbach R, Avila M. 2015 Transition to magnetorotational turbulence in Taylor–Couette flow with imposed azimuthal magnetic field. *New J. Phys.* **17**, 093018. (doi:10.1088/1367-2630/17/9/093018)

49. Abshagen J, von Stamm J, Heise M, Will C, Pfister G. 2012 Localized modulation of rotating waves in Taylor–Couette flow. *Phys. Rev. E* **85**, 056307. (doi:10.1103/PhysRevE.85.056307)

50. Lopez JM, Marques F. 2015 Dynamics of axially localized states in Taylor–Couette flows. *Phys. Rev. E* **91**, 053011. (doi:10.1103/PhysRevE.91.053011)

51. Krueger ER, Gross A, Di Prima RC. 1966 On the relative importance of Taylor-vortex and non-axisymmetric modes in flow between rotating cylinders. *J. Fluid Mech.* **24**, 521–538. (doi:10.1017/S002211206600079X)

52. Langford WF, Tagg R, Kostelich EJ, Swinney HL, Golubitsky M. 1988 Primary instabilities and bicriticality in flow between counter-rotating cylinders. *Phys. Fluids* **31**, 776–785. (doi:10.1063/1.866813)

53. Snyder HA. 1968 Stability of rotating Couette flow. I. Asymmetric waveforms. *Phys. Fluids* **11**, 728–734. (doi:10.1063/1.1691991)

54. Coughlin K, Marcus PS. 1996 Turbulent bursts in Couette–Taylor flow. *Phys. Rev. Lett.* **77**, 2214. (doi:10.1103/PhysRevLett.77.2214)

55. Meseguer A, Mellibovsky F, Avila M, Marques F. 2009 Instability mechanisms and transition scenarios of spiral turbulence in Taylor–Couette flow. *Phys. Rev. E* **80**, 046315. (doi:10.1103/PhysRevE.80.046315)

56. Avila K, Hof B. 2013 High-precision Taylor–Couette experiment to study subcritical transitions and the role of boundary conditions and size effects. *Rev. Sci. Instrum.* **84**, 065106. (doi:10.1063/1.4807704)

57. Cross MC, Hohenberg PC. 1993 Pattern formation outside of equilibrium. *Rev. Mod. Phys.* **65**, 851–1112. (doi:10.1103/RevModPhys.65.851)

58. Cross MC, Greenside H. 2009 *Pattern formation and dynamics in nonequilibrium systems*. Cambridge, UK: Cambridge University Press. (doi:10.1140/epjh/e2010-00003-3)

59. Mallock A. 1889 IV. Determination of the viscosity of water. *Proc. R. Soc. Lond.* **45**, 126–132. (doi:10.1098/rspl.1888.0081)

60. Couette M. 1888 Sur un nouvel appareil pour l'étude du frottement des fluides. *Compt. Rendus des Séances de l'Académie des Sciences (Paris)* **107**, 388–390.

61. Cole JA. 1976 Taylor-vortex instability and annulus-length effects. *J. Fluid Mech.* **75**, 1–15. (doi:10.1017/S0022112076000098)

62. Burin MJ, Ji H, Schartman E, Cutler R, Heitzenroeder P, Liu W, Morris L, Raftopolous S. 2006 Reduction of Ekman circulation within Taylor–Couette flow. *Exp. Fluids* **40**, 962–966. (doi:10.1007/s00348-006-0132-y)

63. Benjamin TB. 1978 Bifurcation phenomena in steady flows of a viscous fluid. I. Theory. *Proc. R. Soc. Lond. A* **359**, 1–26. (doi:10.1098/rspa.1978.0028)

64. Benjamin TB, Mullin T. 1981 Anomalous modes in the Taylor experiment. *Proc. R. Soc. Lond. A.* **377**, 221–249. (doi:10.1098/rspa.1981.0122)

65. Pfister G, Schmidt H, Cliffe KA, Mullin T. 1988 Bifurcation phenomena in Taylor–Couette flow in a very short annulus. *J. Fluid Mech.* **191**, 1–18. (doi:10.1017/S0022112088001491)

66. Mullin T, Toya Y, Tavener SJ. 2002 Symmetry-breaking and multiplicity of states in small aspect ratio Taylor–Couette flow. *Phys. Fluids* **14**, 2778–2787. (doi:10.1063/1.1485997)

67. Pfister G, Buzug T, Enge N. 1992 Characterization of experimental time series from Taylor–Couette flow. *Physica D* **58**, 441–454. (doi:10.1016/0167-2789(92)90130-F)

68. Marques F, Lopez JM. 2006 Onset of three-dimensional unsteady states in small-aspect-ratio Taylor–Couette flow. *J. Fluid Mech.* **561**, 255–277. (doi:10.1017/S0022112006000681)

69. Abshagen J, Lopez JM, Marques F, Pfister G. 2005 Symmetry breaking via global bifurcations of modulated rotating waves in hydrodynamics. *Phys. Rev. Lett.* **94**, 074501. (doi:10.1103/PhysRevLett.94.074501)

70. Heise M, Abshagen J, Küter D, Hochstrate K, Pfister G, Hoffmann C. 2008 Localized spirals in Taylor–Couette flow. *Phys. Rev. E* **77**, 026202. (doi:10.1103/PhysRevE.77.026202)

71. Heise M, Hochstrate K, Abshagen J, Pfister G. 2009 Spirals vortices in Taylor–Couette flow with rotating endwalls. *Phys. Rev. E* **80**, 045301. (doi:10.1103/PhysRevE.80.045301)

72. Crowley CJ, Krygier MC, Borrero-Echeverry D, Grigoriev RO, Schatz MF. 2020 A novel subcritical transition to turbulence in Taylor–Couette flow with counter-rotating cylinders. *J. Fluid Mech.* **892**, A12. (doi:10.1017/jfm.2020.177)

73. Czarny O, Serre E, Bontoux P, Lueptow RM. 2002 Spiral and wavy vortex flows in short counter-rotating Taylor–Couette cells. *Theor. Comput. Fluid Dyn.* **16**, 5–15. (doi:10.1007/s00162-002-0070-0)

74. Böberg L, Brösa U. 1988 Onset of turbulence in a pipe. *Zeitschrift für Naturforschung A* **43**, 697–726. (doi:10.1515/zna-1988-8-901)

75. Hamilton JM, Kim J, Waleffe F. 1995 Regeneration mechanisms of near-wall turbulence structures. *J. Fluid Mech.* **287**, 317–348. (doi:10.1017/S0022112095000978)

76. Hall P, Sherwin S. 2010 Streamwise vortices in shear flows: harbingers of transition and the skeleton of coherent structures. *J. Fluid Mech.* **661**, 178–205. (doi:10.1017/S0022112010002892)

77. Kaneko K. 1985 Spatiotemporal intermittency in coupled map lattices. *Prog. Theor. Phys.* **74**, 1033–1044. (doi:10.1143/PTP.74.1033)

78. Bottin S, Daviaud F, Manneville P, Dauchot O. 1998 Discontinuous transition to spatiotemporal intermittency in plane Couette flow. *Europhys. Lett.* **43**, 171. (doi:10.1209/epl/i1998-00336-3)

79. Feynman RP, Leighton RB, Sands M. 1977 *The Feynman lectures on physics*, vol. 2. Boston, MA: Addison-Wesley.

80. Burin MJ, Czarnocki CJ. 2012 Subcritical transition and spiral turbulence in circular Couette flow. *J. Fluid Mech.* **79**, 106–122. (doi:10.1017/jfm.2012.323)

81. Prigent A, Grégoire G, Chaté H, Dauchot O, van Saarloos W. 2002 Large-scale finite-wavelength modulation within turbulent shear flows. *Phys. Rev. Lett.* **89**, 014501. (doi:10.1103/PhysRevLett.89.014501)

82. Kashyap PV, Duguet Y, Dauchot O. 2022 Linear instability of turbulent channel flow. *Phys. Rev. Lett.* **129**, 244501. (doi:10.1103/PhysRevLett.129.244501)

83. Prigent A, Grégoire G, Chaté H, Dauchot O. 2003 Long-wavelength modulation of turbulent shear flows. *Physica D* **174**, 100–113. (doi:10.1016/S0167-2789(02)00685-1)

84. Avila K, Hof B. 2020 Second-order phase transition in counter-rotating Taylor–Couette flow experiment. *Entropy* **23**, 58. (doi:10.3390/e23010058)

85. Litschke H, Roesner KG. 1998 New experimental methods for turbulent spots and turbulent spirals in the Taylor–Couette flow. *Exp. Fluids* **24**, 201–209. (doi:10.1007/s003480050167)

86. Barkley D, Tuckerman LS. 2005 Computational study of turbulent–laminar patterns in Couette flow. *Phys. Rev. Lett.* **94**, 014502. (doi:10.1103/PhysRevLett.94.014502)

87. Berghout P, Dingemans RJ, Zhu X, Verzicco R, Stevens RJAM, Van Saarloos W, Lohse D. 2020 Direct numerical simulations of spiral Taylor–Couette turbulence. *J. Fluid Mech.* **887**, A18. (doi:10.1017/jfm.2020.33)

88. Tillmark N, Alfredsson PH. 1996 Experiments on rotating plane Couette flow. In *Advances in turbulence VI* (eds S Gavrilakis, L Machiels, PA Monkewitz), Proceedings of the Sixth European Turbulence Conference, pp. 391–394. Boston, MA: Kluwer Academic.

89. Tsukahara T, Tillmark N, Alfredsson PH. 2010 Flow regimes in a plane Couette flow with system rotation. *J. Fluid Mech.* **648**, 5–33. (doi:10.1017/S0022112009993880)

90. Avila M, Grimes M, Lopez JM, Marques F. 2008 Global endwall effects on centrifugally stable flows. *Phys. Fluids* **20**, 104104. (doi:10.1063/1.2996326)

91. Avila M. 2012 Stability and angular-momentum transport of fluid flows between corotating cylinders. *Phys. Rev. Lett.* **108**, 124501. (doi:10.1103/PhysRevLett.108.124501)

92. Lopez JM. 2016 Subcritical instability of finite circular Couette flow with stationary inner cylinder. *J. Fluid Mech.* **793**, 589–611. (doi:10.1017/jfm.2016.146)

93. Kohyama K, Sano M, Tsukahara T. 2022 Sidewall effect on turbulent band in subcritical transition of high-aspect-ratio duct flow. *Phys. Fluids* **34**, 084112. (doi:10.1063/5.0096626)

94. Wu H, Song B. 2022 A numerical study of the side-wall effects on turbulent bands in channel flow at transitional Reynolds numbers. *Comput. Fluids* **240**, 105420. (doi:10.1016/j.compfluid.2022.105420)

95. Borrero-Echeverry D, Schatz MF, Tagg R. 2010 Transient turbulence in Taylor–Couette flow. *Phys. Rev. E* **81**, 025301. (doi:10.1103/PhysRevE.81.025301)

96. Peixinho J, Mullin T. 2006 Decay of turbulence in pipe flow. *Phys. Rev. Lett.* **96**, 094501. (doi:10.1103/PhysRevLett.96.094501)

97. Hof B, Westerweel J, Schneider TM, Eckhardt B. 2006 Finite lifetime of turbulence in shear flows. *Nature* **443**, 59–62. (doi:10.1038/nature05089)

98. Hof B, de Lozar A, Kuik DJ, Westerweel J. 2008 Repeller or attractor? Selecting the dynamical model for the onset of turbulence in pipe flow. *Phys. Rev. Lett.* **101**, 214501. (doi:10.1103/PhysRevLett.101.214501)

99. Avila M, Willis AP, Hof B. 2010 On the transient nature of localized pipe flow turbulence. *J. Fluid Mech.* **646**, 127–136. (doi:10.1017/S0022112009993296)

100. Alidai A, Greidanus AJ, Delfos R, Westerweel J. 2016 Turbulent spot in linearly stable Taylor–Couette flow. *Flow Turbul. Combust.* **96**, 609–619. (doi:10.1007/s10494-015-9664-7)

101. Goldenfeld N, Guttenberg N, Gioia G. 2010 Extreme fluctuations and the finite lifetime of the turbulent state. *Phys. Rev. E* **81**, 035304(R). (doi:10.1103/PhysRevE.81.035304)

102. Gumbel EJ. 1958 *Statistics of extremes*. New York, NY: Columbia University Press.

103. Nemoto T, Alexakis A. 2021 Do extreme events trigger turbulence decay? A numerical study of turbulence decay time in pipe flows. *J. Fluid Mech.* **912**, A38. (doi:10.1017/jfm.2020.1150)

104. Gomé S, Tuckerman LS, Barkley D. 2022 Extreme events in transitional turbulence. *Phil. Trans. R. Soc. A* **380**, 20210036. (doi:10.1098/rsta.2021.0036)

105. Moxey D, Barkley D. 2010 Distinct large-scale turbulent–laminar states in transitional pipe flow. *Proc. Natl Acad. Sci. USA* **107**, 8091–8096. (doi:10.1073/pnas.0909560107)

106. Avila K, Moxey D, De Lozar A, Avila M, Barkley D, Hof B. 2011 The onset of turbulence in pipe flow. *Science* **333**, 192–196. (doi:10.1126/science.1203223)

107. Shi L, Avila M, Hof B. 2013 Scale invariance at the onset of turbulence in Couette flow. *Phys. Rev. Lett.* **110**, 204502. (doi:10.1103/PhysRevLett.110.204502)

108. Lemoult G, Shi L, Avila K, Jalikop SV, Avila M, Hof B. 2016 Directed percolation phase transition to sustained turbulence in Couette flow. *Nat. Phys.* **12**, 254. (doi:10.1038/nphys3675)

109. Tuckerman LS, Chantry M, Barkley D. 2020 Patterns in wall-bounded shear flows. *Annu. Rev. Fluid Mech.* **52**, 343–367. (doi:10.1146/annurev-fluid-010719-060221)

110. Hof B. 2022 Directed percolation and the transition to turbulence. *Nat. Rev. Phys.* **5**, 62–72. (doi:10.1038/s42254-022-00539-y)

111. Nagata M. 1990 Three-dimensional finite-amplitude solutions in plane Couette flow: bifurcation from infinity. *J. Fluid Mech.* **217**, 519–527. (doi:10.1017/S0022112090000829)

112. Kreilos T, Eckhardt B. 2012 Periodic orbits near onset of chaos in plane Couette flow. *Chaos* **22**, 047505. (doi:10.1063/1.4757227)

113. Clever RM, Busse FH. 1997 Tertiary and quaternary solutions for plane Couette flow. *J. Fluid Mech.* **344**, 137–153. (doi:10.1017/S0022112097005818)

114. Romanov VA. 1973 Stability of plane-parallel Couette flow. *Funct. Anal. Appl.* **7**, 137–146. (doi:10.1007/BF01078886)

115. Lustro JRT, Kawahara G, van Veen L, Shimizu M, Kokubu H. 2019 The onset of transient turbulence in minimal plane Couette flow. *J. Fluid Mech.* **862**, R2. (doi:10.1017/jfm.2018.971)

116. Grebogi C, Ott E, Yorke JA. 1983 Crises, sudden changes in chaotic attractors, and transient chaos. *Physica D* **7**, 181–200. (doi:10.1016/0167-2789(83)90126-4)

117. Kreilos T, Eckhardt B, Schneider TM. 2014 Increasing lifetimes and the growing saddles of shear flow turbulence. *Phys. Rev. Lett.* **112**, 044503. (doi:10.1103/PhysRevLett.112.044503)

118. Meseguer A, Mellibovsky F, Avila M, Marques F. 2009 Families of subcritical spirals in highly counter-rotating Taylor–Couette flow. *Phys. Rev. E* **79**, 036309. (doi:10.1103/PhysRevE.79.036309)

119. Deguchi K, Meseguer A, Mellibovsky F. 2014 Subcritical equilibria in Taylor–Couette flow. *Phys. Rev. Lett.* **112**, 184502. (doi:10.1103/PhysRevLett.112.184502)

120. Wang B, Ayats R, Deguchi K, Mellibovsky F, Meseguer A. 2022 Self-sustainment of coherent structures in counter-rotating Taylor–Couette flow. *J. Fluid Mech.* **951**, A21. (doi:10.1017/jfm.2022.828)

121. Reetz F, Kreilos T, Schneider TM. 2019 Invariant solution underlying oblique stripe patterns in plane Couette flow. *Nat. Commun.* **10**, 2277. (doi:10.1038/s41467-019-10208-x)

122. Kawahara G, Kida S. 2001 Periodic motion embedded in plane Couette turbulence: regeneration cycle and burst. *J. Fluid Mech.* **449**, 291–300. (doi:10.1017/S0022112001006243)

123. Gibson JF, Halcrow J, Cvitanović P. 2008 Visualizing the geometry of state space in plane Couette flow. *J. Fluid Mech.* **611**, 107–130. (doi:10.1017/S002211200800267X)

124. Graham MD, Floryan D. 2021 Exact coherent states and the nonlinear dynamics of wall-bounded turbulent flows. *Annu. Rev. Fluid Mech.* **53**, 227–253. (doi:10.1146/annurev-fluid-051820-020223)

125. Kawahara G, Uhlmann M, Van Veen L. 2012 The significance of simple invariant solutions in turbulent flows. *Annu. Rev. Fluid Mech.* **44**, 203–225. (doi:10.1146/annurev-fluid-120710-101228)

126. Krygier MC, Pughe-Sanford JL, Grigoriev RO. 2021 Exact coherent structures and shadowing in turbulent Taylor–Couette flow. *J. Fluid Mech.* **923**, A7. (doi:10.1017/jfm.2021.522)

127. Crowley CJ, Pughe-Sanford JL, Toler W, Krygier MC, Grigoriev RO, Schatz MF. 2022 Turbulence tracks recurrent solutions. *Proc. Natl Acad. Sci. USA* **119**, e2120665119. (doi:10.1073/pnas.2120665119)

128. Crowley C, Pughe-Sanford J, Toler W, Grigoriev R, Schatz M. 2023 Observing a dynamical skeleton of turbulence in Taylor–Couette flow experiments. *Phil. Trans. R. Soc. A* **381**, 20220137. (doi:10.1098/rsta.2022.0137)

129. Deguchi K. 2017 Linear instability in Rayleigh-stable Taylor–Couette flow. *Phys. Rev. E* **95**, 021102. (doi:10.1103/PhysRevE.95.021102)

130. Pringle JE. 1981 Accretion discs in astrophysics. *Annu. Rev. Astron. Astrophys.* **19**, 137–160. (doi:10.1146/annurev.aa.19.090181.001033)

131. Papaloizou J, Lin D. 1995 Theory of accretion disks I: angular momentum transport processes. *Annu. Rev. Astron. Astrophys.* **33**, 505–540. (doi:10.1146/annurev.aa.33.090195.002445)

132. Soward AM, Jones CA, Hughes DW, Weiss NO. 2005 *Fluid dynamics and dynamos in astrophysics and geophysics*. Boca Raton, FL: CRC Press.

133. Balbus SA. 2003 Enhanced angular momentum transport in accretion disks. *Annu. Rev. Astron. Astrophys.* **41**, 555–597. (doi:10.1146/annurev.astro.41.081401.155207)

134. Ji H, Burin M, Schartman E, Goodman J. 2006 Hydrodynamic turbulence cannot transport angular momentum effectively in astrophysical disks. *Nature* **444**, 343–346. (doi:10.1038/nature05323)

135. Paoletti MS, Lathrop DP. 2011 Angular momentum transport in turbulent flow between independently rotating cylinders. *Phys. Rev. Lett.* **106**, 024501. (doi:10.1103/PhysRevLett.106.024501)

136. Edlund EM, Ji H. 2014 Nonlinear stability of laboratory quasi-Keplerian flows. *Phys. Rev. E* **89**, 021004. (doi:10.1103/PhysRevE.89.021004)

137. Lopez JM, Avila M. 2017 Boundary-layer turbulence in experiments on quasi-Keplerian flows. *J. Fluid Mech.* **817**, 21–34. (doi:10.1017/jfm.2017.109)

138. Ostilla-Mónico R, Verzicco R, Grossmann S, Lohse D. 2014 Turbulence decay towards the linearly stable regime of Taylor–Couette flow. *J. Fluid Mech.* **748**, R3. (doi:10.1017/jfm.2014.242)

139. Shi L, Hof B, Rampp M, Avila M. 2017 Hydrodynamic turbulence in quasi-Keplerian rotating flows. *Phys. Fluids* **29**, 044107. (doi:10.1063/1.4981525)

140. Ji H, Goodman J. 2023 Taylor–Couette flow for astrophysical purposes. *Phil. Trans. R. Soc. A* **381**, 20220119. (doi:10.1098/rsta.2022.0119)

141. Guseva A, Tobias S. 2023 Transition to chaos and modal structure of magnetized Taylor–Couette flow. *Phil. Trans. R. Soc. A* **381**, 20220120. (doi:10.1098/rsta.2022.0120)

142. Canton J, Rinaldi E, Örlü R, Schlatter P. 2020 Critical point for bifurcation cascades and featureless turbulence. *Phys. Rev. Lett.* **124**, 014501. (doi:10.1103/PhysRevLett.124.014501)

143. Feldmann D, Borrero-Echeverry D, Burin MJ, Avila K, Avila M. 2023 Routes to turbulence in Taylor–Couette flow. PANGAEA. (https://doi.pangaea.de/10.1594/PANGAEA.955328)

144. Feldmann D, Borrero-Echeverry D, Burin MJ, Avila K, Avila M. 2023 Routes to turbulence in Taylor–Couette flow. Figshare. (doi:10.6084/m9.figshare.c.6412312)